NOAA Technical Report NESS 88

Observations of Hurricane David (1979) Using the Microwave Sounding Unit

Washington, D.C.
April 1982

U.S. DEPARTMENT OF COMMERCE
National Oceanic and Atmospheric Administration
National Earth Satellite Service

NOAA TECHNICAL REPORTS

National Earth Satellite Service Series

The National Earth Satellite Service (NESS) is responsible for the establishment and operation of the environmental satellite systems of NOAA.

Publication of a report in NOAA Technical Report NESS series will not preclude later publication in an expanded or modified form in scientific journals. NESS series of NOAA Technical Reports is a continuation of, and retains the consecutive numbering sequence of, the former series, ESSA Technical Report National Environmental Satellite Center (NESC), and of the earlier series, Weather Bureau Meteorological Satellite Laboratory (MSL) Report. Reports 1 through 39 are listed in publication NESC 56 of this series.

Reports in the series are available from the National Technical Information Service (NTIS), U.S. Department of Commerce, Sills Bldg., 5285 Port Royal Road, Springfield, VA 22161, in paper copy or microfiche form. Order by accession number, when given, in parentheses. Beginning with 64, printed copies of the reports, if available, can be ordered through the Superintendent of Documents, U.S. Government Printing Office, Washington, DC 20402. Prices given on request from the Superintendent of Documents or NTIS.

ESSA Technical Reports

NESC 46 Monthly and Seasonal Mean Global Charts of Brightness From ESSA 3 and ESSA 5 Digitized Pictures, February 1967-February 1968. V. Ray Taylor and Jay S. Winston, November 1968, 9 pp. plus 17 charts. (PB-180-717)

NESC 47 A Polynomial Representation of Carbon Dioxide and Water Vapor Transmission. William L. Smith, February 1969 (reprinted April 1971), 20 pp. (PB-183-296)

NESC 48 Statistical Estimation of the Atmosphere's Geopotential Height Distribution From Satellite Radiation Measurements. William L. Smith, February 1969, 29 pp. (PB-183-297)

NESC 49 Synoptic/Dynamic Diagnosis of a Developing Low-Level Cyclone and Its Satellite-Viewed Cloud Patterns. Harold J. Brodrick and E. Paul McClain, May 1969, 26 pp. (PB-184-612)

NESC 50 Estimating Maximum Wind Speed of Tropical Storms From High Resolution Infrared Data. L. F. Hubert, A. Timchalk, and S. Fritz, May 1969, 33 pp. (PB-184-611)

NESC 51 Application of Meteorological Satellite Data in Analysis and Forecasting. Ralph K. Anderson, Jerome P. Ashman, Fred Bittner, Golden R. Farr, Edward W. Ferguson, Vincent J. Oliver, Arthur H. Smith, James F. W. Purdom, and Rance W. Skidmore, March 1974 (reprint and revision of NESC 51, September 1969, and inclusion of Supplement, November 1971, and Supplement 2, March 1973), pp. 1--6C-18 plus references.

NESC 52 Data Reduction Processes for Spinning Flat-Plate Satellite-Borne Radiometers. Torrence H. MacDonald, July 1970, 37 pp. (COM-71-00132)

NESC 53 Archiving and Climatological Applications of Meteorological Satellite Data. John A. Leese, Arthur L. Booth, and Frederick A. Godshall, July 1970, pp. 1-1--5-8 plus references and appendixes A through D. (COM-71-00076)

NESC 54 Estimating Cloud Amount and Height From Satellite Infrared Radiation Data. P. Krishna Rao, July 1970, 11 pp. (PB-194-685)

NESC 56 Time-Longitude Sections of Tropical Cloudiness (December 1966-November 1967). J. M. Wallace, July 1970, 37 pp. (COM-71-00131)

NOAA Technical Reports

NESS 55 The Use of Satellite-Observed Cloud Patterns in Northern Hemisphere 500-mb Numerical Analysis. Roland E. Nagle and Christopher M. Hayden, April 1971, 25 pp. plus appendixes A, B, and C. (COM-73-50262)

NESS 57 Table of Scattering Function of Infrared Radiation for Water Clouds. Giichi Yamamoto, Masayuki Tanaka, and Shoji Asano, April 1971, 8 pp. plus tables. (COM-71-50312)

NESS 58 The Airborne ITPR Brassboard Experiment. W. L. Smith, D. T. Hilleary, E. C. Baldwin, W. Jacob, H. Jacobowitz, G. Nelson, S. Soules, and D. Q. Wark, March 1972, 74 pp. (COM-72-10557)

NESS 59 Temperature Sounding From Satellites. S. Fritz, D. Q. Wark, H. E. Fleming, W. L. Smith, H. Jacobowitz, D. T. Hilleary, and J. C. Alishouse, July 1972, 49 pp. (COM-72-50963)

NESS 60 Satellite Measurements of Aerosol Backscattered Radiation From the Nimbus F Earth Radiation Budget Experiment. H. Jacobowitz, W. L. Smith, and A. J. Drummond, August 1972, 9 pp. (COM-72-51031)

(Continued on inside back cover)

NOAA Technical Report NESS 88

Observations of Hurricane David (1979) Using the Microwave Sounding Unit

Norman C. Grody and William C. Shen

Washington, D.C.
April 1982

U. S. DEPARTMENT OF COMMERCE
Malcolm Baldrige, Secretary
National Oceanic and Atmospheric Administration
John V. Byrne, Administrator
National Earth Satellite Service
John H. McElroy, Assistant Administrator for Satellites

CONTENTS

FIGURES

Observations of Hurricane David (1979) using the Microwave Sounding Unit

Norman C. Grody and William C. Shen
National Earth Satellite Service, NOAA
Washington, D.C.

Abstract. The Microwave Sounding Unit was first launched October 13, 1978, aboard TIROS-N, as a component of an operational sounding system. The sounder consists of four oxygen channels (50.30, 53.74, 54.96, 57.95 GHz) with a horizontal resolution of 110 km at nadir. This study reports on the microwave measurements obtained for Hurricane David at four 12-h intervals, beginning September 3, 1979, when David was in the Florida Strait, until 48-h later when it approached the Georgia coast.

Comparisons are made between the brightness temperature measurements for the three highest frequency channels (called "sounding" channels) and the values computed from radiosonde data. Precipitation effects are only evident in the lowest peaking (700 mb) sounding channel at 53.74 GHz. At 54.96 GHz, the measurements display the magnitude and spatial extent of the hurricanes warm-core anomaly near 300 mb. The highest sounding channel at 57.95 GHz responds to temperatures around 100 mb and displays a strong north-south gradient corresponding to the latitudinal variation in tropopause height. For this channel, the influence of the hurricane appears minimal, although there is a greater disparity with the radiosonde computations than for the lower sounding channels.

In addition to the individual spot measurements, comparisons are also made between the radial derivative of brightness temperature for the 54.96-GHz channel and the derivatives estimated using radiosonde winds. Measurements and simulations demonstrate that the brightness temperature derivative is correlated with the winds between 700 and 500 mb. Horizontal smoothing resulting from the instrument's 110-km resolution degrades the gradient information near the hurricane center more than the spot measurements of brightness temperature.

1. INTRODUCTION

Of the various meteorological events monitored by satellite instruments, perhaps the most intriguing is that of tropical storms. These events have been studied using sensors that provide visible, infrared, and microwave images (e.g., Fritz et al., 1966; Dvorak, 1975; Allison et al., 1974). However, unlike the visible and infrared observations, microwaves are capable of penetrating the cirrus canopy and probing the inner core of tropical storms.

The cloud penetrating property of microwave radiation was demonstrated in the studies of Typhoon June using the five-channel (22.23, 31.65, 52.85, 53.85, 55.45 GHz) Scanning Microwave Spectrometer (SCAMS) aboard the polar orbiting

Nimbus-6 satellite. Atmospheric liquid water, precipitable water, and sea surface winds were derived using the 22.23-GHz water vapor channel and 31.65-GHz window channel measurements (Rosenkranz et al., 1978). The 55.45-GHz SCAMS oxygen channel (whose temperature weighting function peaks near 200 mb) was used to display the storm's warm-core temperature structure. In other studies of Typhoon June, the central pressure was derived (Kidder et al., 1978), and the tangential winds near 700 mb were estimated (Grody et al., 1979) using this upper tropospheric sounding channel. However, underestimates of the temperaure anomaly and tangential winds were observed near the storm center, and these were attributed to the SCAMS maximum horizontal resolution of only 146 km (nadir).

Less is known concerning the application of the lower tropospheric oxygen channels (less than 55 GHz) in convective systems since both temperature and liquid water can influence the response. In the midlatitudes, the large variations in temperature generally exceed that due to liquid water (Grody and Pellegrino, 1977). However, in the tropics, the liquid water effects can dominate the response of the lower tropospheric channels (Hubert et al., 1981). For example, the 52.85- and 53.85-GHZ SCAMS channels, whose temperature weighting functions peak below 500 mb, could not readily be used to study the thermal structure of Typhoon June because of liquid water attenuation. Such lower-probing oxygen channels may be useful in estimating the amount and vertical extent of liquid water (Rosenkranz et al., 1972) once the influence of temperature is removed. In addition to the applications of the oxygen channels referred to above, this study examines the possibility of using them for liquid water determination.

Rather than use the SCAMS instrument, which was limited to about 1 year of continuous operation prior to failure of the scan mechanism during May 1976, it appeared more advantageous to apply the currently available Microwave Sounding Unit in a detailed study of Hurricane David (1979). This storm was chosen because of the relatively large amount of radiosonde and radar data available for comparison with the microwave measurements. The sounder's brightness temperature measurements at 53.74, 54.96, and 57.95 GHz are compared with radiosonde computations. Precipitation effects are determined using the radar data and the radiosonde comparisons. Simulations are used to generate retrieval algorithms for temperature and winds and to model the effects of liquid water attenuation on the brightness temperatures. The temperatures and winds derived from the microwave measurements are then compared with the radiosonde data.

2. THE MICROWAVE SOUNDING UNIT

The Microwave Sounding Unit (MSU) is a component of an operational sounding system and was designed to (a) produce global soundings under nearly all weather conditions (Grody, 1980) and (b) to complement the infrared sounder which contains more channels but is limited to clearer atmospheres (Smith et al., 1979). First launched on October 13, 1978, aboard the polar orbiting TIROS-N satellite (later aboard NOAA satellites), the MSU is similar to the SCAMS instrument, with differences mainly in channel selection and scan geometry.

2.1 Instrument Description

The sounder consists of four individual Dicke-type radiometers to detect thermal radiation in the oxygen band at 50.30, 53.74, 54.96, and 57.95 GHz. A crosstrack rotating reflector directs the incoming radiation through a fixed circular horn which is coupled to the radiometers. Front-end loss from frequency multiplexing is reduced using two separate antennas (reflector + horn), one for the 50.30- and 53.74-GHz channels and a second for the remaining channels. The antenna beamwidths are both set to 7.5° by the reflector dimensions (same as SCAMS). This results in a 3-dB footprint at nadir of 110 km, which is less than that of SCAMS (146 km) due to the lower orbit of TIROS-N compared to Nimbus-6. To scan the Earth in 25.6 s, the reflector rotates with 11 equal angular increments of 9.5° as shown in figure 1. (SCAMS had 13 steps with 7.2° increments for greater sampling.) Two additional steps not shown in figure 1 provide calibration views of cold space and an ambient-temperature target attached to the scan structure. Ground-based data processing results in individually calibrated brightness temperatures for the four channels using a nearly linear relationship between the output channel response to the monitored target temperature and the 2.7 K cold-space temperature.

Fluctuations in the brightness temperature measurements (noise) are limited to about 0.25 K by the 1.85-s integration time per spot and 200-MHz predetection bandwidth of the channels. The MSU integration time is double that of SCAMS, resulting in a 40 percent reduction of noise temperature. The reduced noise and greater resolution of the MSU compared to SCAMS are particularly advantageous when observing the small-amplitude, subsynoptic features associated with tropical storms.

2.2 Channel Characteristics

It is appropriate to begin this discussion with the brightness temperature relationship for clear atmospheres, followed by an examination of cloud and precipitation effects for the MSU channels. A somewhat more compact notation is introduced for expressing the brightness temperature, and is briefly described below.

For a nonscattering atmosphere, the brightness temperature $T_B(\nu)$ at frequency ν can be related to the atmospheric temperature profile T(p) by introducing an "effective transmittance function", $\tau_\nu(p)$, viz;

$$T_B(\nu) = \int_{\ln p_s}^{-\infty} T(p) \frac{d\tau_\nu(p)}{d\ln p} \, d\ln p + \tau_\nu(p_s) T_s \qquad (1a)$$

where

$$\tau_\nu(p) = \left[1 - \left(\frac{\hat{\tau}_\nu(p_s)}{\hat{\tau}_\nu(p)} \right)^{2\mathrm{Sec}\theta} \left(1-\varepsilon_s(\nu,\theta)\right) \right] \hat{\tau}_\nu(p)^{\mathrm{Sec}\theta} \qquad (1b)$$

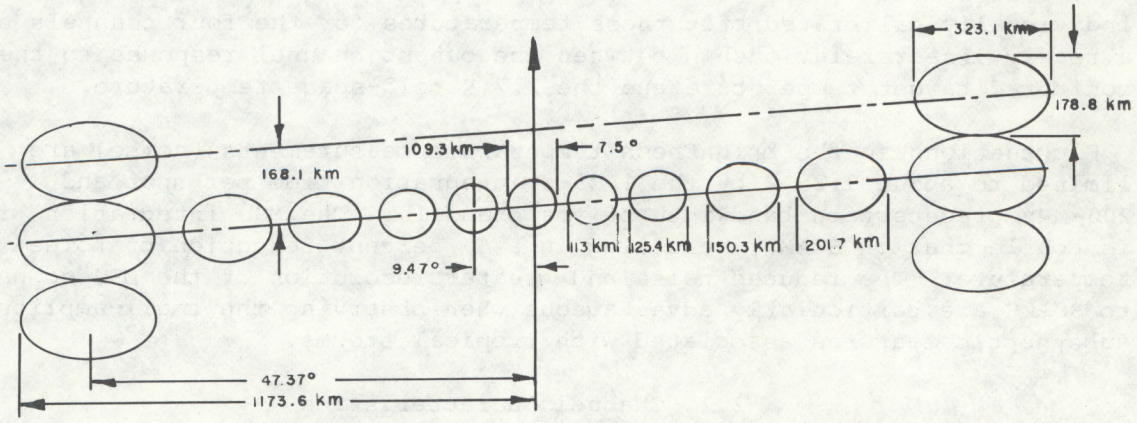

MICROWAVE SOUNDING UNIT

SCAN PATTERN PROJECTED ON EARTH

(833.4 km CIRCULAR ORBIT)

Figure 1. MSU scan grid pattern and field of view (half power) projected on Earth.

The effective transmittance combines the relatively temperature-independent parameters of the radiative transfer equation into a single function. It contains the familiar transmittance function $\hat{\tau}_\nu(p)$, the exponential absorption along the vertical path beginning at the satellite level and terminating at pressure p. For the frequencies of interest, the absorption is mainly due to molecular oxygen. As the instrument scans from nadir, the longer paths through the atmosphere increase the absorption, where this "limb effect" is accounted for by the Sec θ term; θ is the Earth-located zenith angle which has the values, of 0^o, $\pm$ 10.7^o, $\pm$ 21.6^o, $\pm$ 32.7^o, $\pm$ 44.2^o, $\pm$ 56.6^o for the 11 scan positions. The nonunity term in brackets in eq. (1b) accounts for the surface reflected brightness temperature contribution, where $\varepsilon_s(\nu,\theta)$ is the surface emissivity. The magnitude of this term depends on the surface type since the emissivity varies from near unity for dry land to about 0.5 for sea surfaces for the MSU channels. Also contained in eq. (1) is the surface temperature Ts, surface pressure p_s, and the transmittance along the complete vertical path $\hat{\tau}_\nu(p_s)$.

The kernel $-d\tau_\nu(p)/d \ln p$ in eq. (1a) is called the temperature weighting function since it defines the contribution of temperature at different altitudes to the brightness temperature. Figure 2 shows the weighting functions for the MSU channels; these were calculated using Rosenkranz's oxygen absorption model (1975) and Liebe's line width parameters (1977). The functions are shown for dry land ($\varepsilon_s = 1.0$) and a smooth sea surface ($\varepsilon_s = 0.5$), when viewed at nadir ($\theta = 0^o$) and the extreme viewing angle ($\theta = 56.6^o$). Observe that the distributions peak higher in the atmosphere as the frequency approaches the center of the oxygen band at 60 GHz. For example, at nadir the 50.30-GHz channel peaks below the surface while the next higher frequency channel (53.74 GHz) peaks in the lower troposphere at 700 mb. Also, at nadir the 54.96-GHz channel is centered at 300 mb (mean tropopause in midlatitudes), while the highest-frequency channel (57.95 GHz) peaks near the mean tropical tropopause of 100 mb. Although the weighting functions are largely defined by the channel frequencies, the effects of scanning and surface emissivity are also apparent and must be accounted for.

2.2.1 Scanning and surface emissivity effects

As shown in figure 2, the weighting functions are elevated due to angular scanning by virtue of the limb effect discussed above. For the extreme scan angle, the limb effect produces almost a 30 percent decrease in the pressure at which all the weighting functions peak. In general, if $p(0^o)$ is the pressure at which a weighting function peaks at nadir, then, for an arbitrary zenith angle, the pressure is approximately given by $p(\theta) = p(0^o)\sqrt{\cos\theta}$. There are various ways of treating the limb effect; i.e., the brightness temperatures can be corrected prior to their use, or the geophysical algorithms can include the effect. Since this study involves the interpretation of the brightness temperature measurements, it is advantageous to examine the data in the limb corrected form.

A limb correction procedure was developed by Smith et al. (1974) using regression analysis to relate the nadir brightness temperature of a channel to the linear combination of all channel measurements at a particular scan angle. Synthesized brightness temperatures computed from a climatological

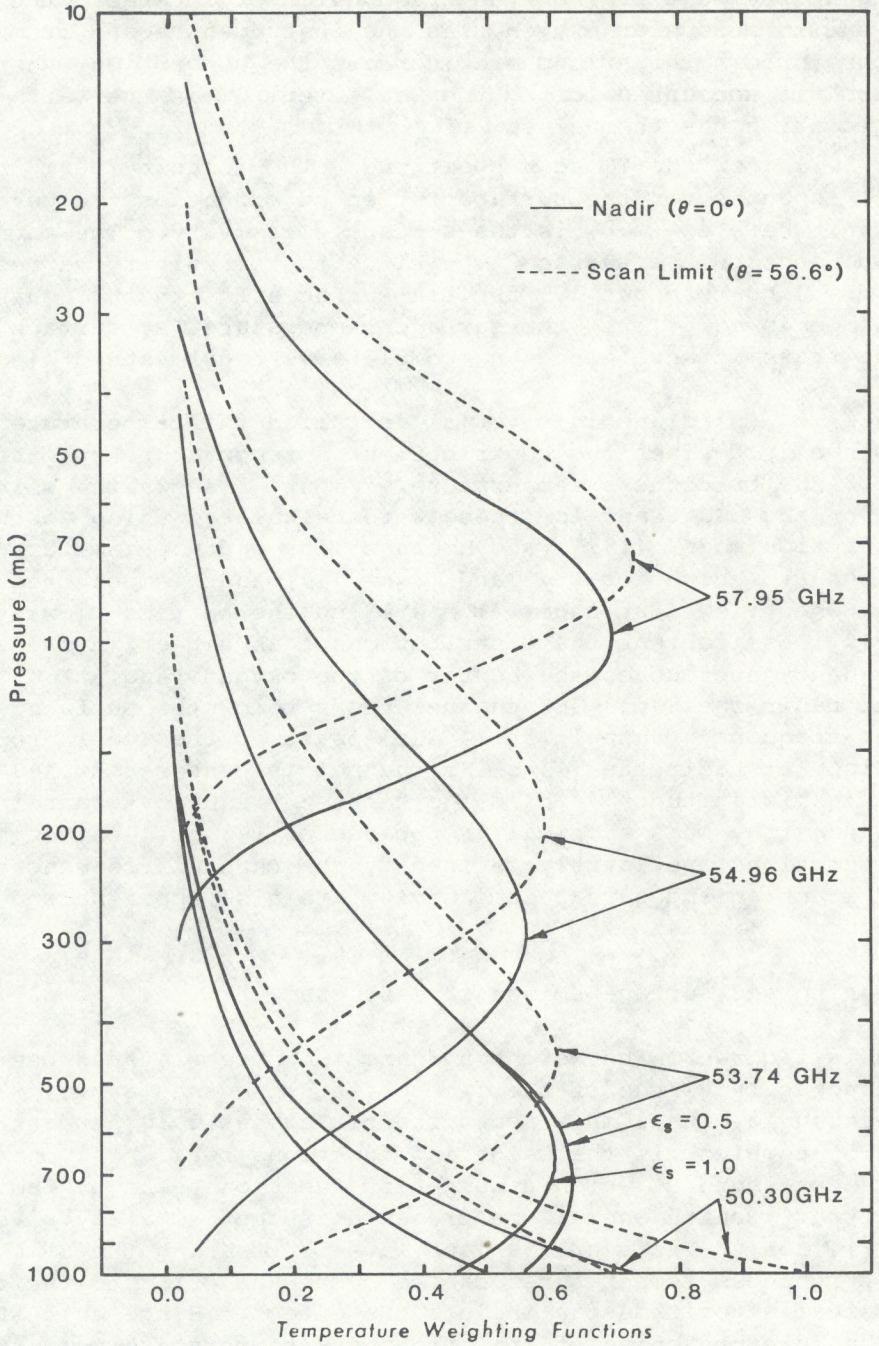

Figure 2. MSU temperature weighting functions calculated for nadir and scan limit positions. Weighting functions are shown for land (ε_s=1) and sea type surfaces (ε_s=0.5).

set of atmospheres are used to derive the regression equations. The procedure physically acts to construct a nadir weighting function from the superposition of off-nadir functions using all channels and incorporates statistical correlations between the two sets of brightness temperatures. As discussed below, this same approach is also used to normalize the brightness temperature (excluding the 50.30-GHz channel) to a unity emissivity surface by generating separate regression coefficients for variable land and sea surfaces. This method of normalizing the measurements to nadir (and unity emissivity) is used operationally and will be applied in this study. An alternate technique of utilizing constant empirical adjustments for each scan position can provide similar results in the tropics where the vertical temperature structure is nearly constant (Rosenkranz et al., 1978). However, the full statistical method of Smith et al. (1974), which incorporates all channels in determining the limb corrections for a given channel, is expected to be more accurate outside the tropics.

In addition to the frequency and zenith-angle dependence, the weighting functions in figure 2 also display an effect of emissivity. The smaller emissivity for sea surfaces compared to land is seen to increase the weighting functions near the surface. This is also evident by referring to eq. (1b) and noting that the emissivity term has increasingly larger contributions as $\hat{\tau}_\nu(p_s)/\hat{\tau}_\nu(p)$ approaches unity for pressures near the surface. The surface effect is particularly noticeable for the most transparent channel (50.30 GHz) whose clear-column transmittance $\hat{\tau}_\nu(p_s)$ is computed to be about 0.7 and less evident for the more opaque channel (53.74 GHz) whose corresponding transmittance is only 0.1. Based on eq. (1) and considering an isothermal atmosphere, the difference in brightness temperature between land and sea type surfaces is $\frac{1}{2}T_s\hat{\tau}_\nu(p_s)^{2\mathrm{Sec}\theta}$. At nadir, using the above transmittance values and an average surface temperature of 285 K, one obtains a 70 K difference for the 50.30-GHz channel and only a 1.4 K difference at 53.74 GHz. Although these values are reduced by limb effects and liquid water attenuation, they indicate a large surface contribution for the most transparent channel and almost insignificant effects for the more opaque channel. The 50.30-GHz channel therefore serves as a "window" channel, being highly sensitive to surface emissivity variations.[1] As such, the 50.30-GHz channel can only be corrected for limb effects. However, the other channels, being more opaque to the surface and less influenced by clouds, can be corrected for both limb effects and emissivity effects by generating separate regression coefficients for land and sea surfaces. The 50.30-GHz measurement is used as a land-ocean discriminator as part of this procedure; a brightness temperature in excess of 265 K is used in this study to indicate land.

From the above discussion, it is clear that the 53.74-, 54.96-, and 57.95-GHz channels are essentially independent of surface effects, having only small perturbations at the lowest correctable frequency. The limb effects are also well understood and correctable from a-priori information. It is therefore possible to consider the weighting functions normalized to nadir and unity emissivity when using the limb corrected brightness temperatures. According to eq. (1a) and the weighting function concept, the

1 Earlier studies (Grody, 1976) also showed the 50-GHz channel and the SCAMS 31-GHz channel to have similar sensitivity to liquid water over sea surfaces.

brightness temperatures for these three "temperature sounding" channels respond to temperatures in the lower troposphere to the lower stratosphere. This is in contrast to the 50.30-GHz window channel which does not have a well defined weighting function as a result of the large emissivity and liquid water effects which cannot be adequately corrected from a-priori information. It is well known that the sounding channel measurements provide estimates of the temperature profile by inverting eq. (1a) using statistical techniques. Temperature profiles have been obtained from MSU measurements under nearly all weather conditions (e.g., Grody ,1980). However, a major exception occurs for tropical storms and squall lines in the midlatitudes, both of which contain extensive areas of thick cloud and precipitation. As shown below, precipitating type clouds, which essentially saturate the window channel measurements, also produce a significant decrease in the lower peaking sounding channel (53.74 GHz), but have a negligible effect on the higher peaking channels.

2.2.2 Liquid water effects (simulated)

Model calculations are performed for the MSU channels to examine their sensitivity to liquid water. Brightness temperatures are determined for both clear and cloudy atmospheres using eq. (1). In the case of a clear atmosphere, the transmittance function $\hat{\tau}(p)$ is the product of the oxygen and water vapor transmittances. In simulating cloudy atmospheres, this clear transmittance function is multiplied by the transmittance component of liquid water. For nonprecipitating clouds, the dropsize is small compared to the 0.5-cm radiation wavelength so that the Rayleigh absorption model is applicable. The effects of precipitation are approximated by neglecting scattering and using eq. (1) with an absorption model for raindrops based on the Marshall-Palmer drop-size distribution (Paris, 1971). Note that although scattering effects of large drops are generally important for window channels (Savage and Weinman, 1975; Ishumaru and Cheung, 1980), the effect is less important for the more opaque oxygen channels. Even for the most transparant MSU channel at 50.30 GHz, one expects the brightness temperature to be dominated by the absorption effects of large drops.

The MSU brightness temperatures at nadir were computed for a mean tropical sounding with a sea surface background ($\varepsilon_s = 0.5$). All results are shown relative to the clear atmosphere. Deep layers of clouds and convection around hurricanes are modeled by introducing a layer of liquid water between the 1000 mb surface and 300 mb level. The cloudy minus clear brightness temperatures were computed for a range of liquid water densities (0 to 0.7 g/m^3). To account for the general decrease of liquid water above the freezing level (600 mb), the density was reduced above this level by an exponential factor, Exp[0.117(T - 273)], based on data presented by Feigelson (1966).

The cloudy minus clear brightness temperatures for the 50.30-, 53.74-, and 54.96-GHz channels are plotted in figure 3 against the liquid water in the column for both nonprecipitating and precipitating clouds. Note that the negative scale on the right is for the sounding channels. Relative to the clear atmosphere, the 50.30-GHz brightness temperature increases while the brightness temperatures of the sounding channels decrease with liquid water. Even under the extreme case of 4 mm of precipitation, the 54.96-GHz channel appears relatively unperturbed. No effects were observed for the highest peaking sounding channel (not shown). The larger effects at 50.30 and 53.74 GHz are now discussed in the following paragraphs.

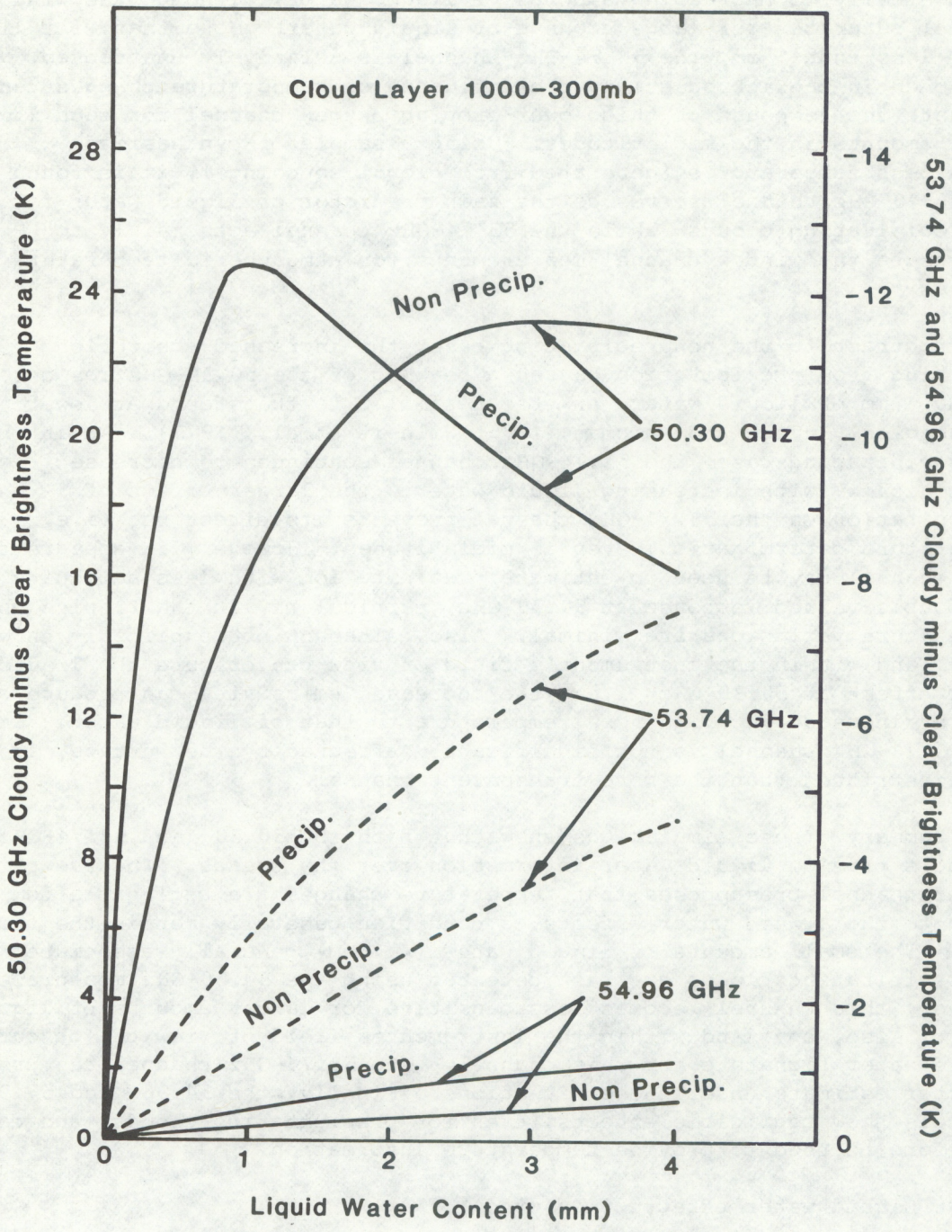

Figure 3. Simulated liquid water effects on MSU channels (50.30, 53.74, 54.96 GHz). Cloudy minus clear brightness temperature values are plotted against liquid water content. Results are shown separately for large drops (precip.) and small drops (non precip.) which are distributed from the sea surface to 300-mb level. (See text for details.)

For nonprecipitating clouds, both channels (50.30 and 53.74 GHz) respond monotonically to increasing amounts of liquid water, although the window channel saturates for large amounts of liquid water. Note that, for liquid water less than 1 mm, the 53.74-GHz channel is relatively unaffected. As mentioned in the introduction, the influence of temperature changes can dominate the response of this lower-probing oxygen channel for such liquid water amounts in the midlatitudes. Using a sample of synthesized brightness temperatures (generated from global soundings), it is found that the 50.30-GHz channel serves as the main predictor of liquid water for nonprecipitating clouds[2] while the 53.74-GHz channel acts mainly to compensate the window channel measurements for atmospheric temperature changes.

In contrast to the nonprecipiating case, the increased absorption resulting from precipitation causes a peaking of the 50.30-GHz response around 1 mm of liquid water, an effect similar to that found at lower frequencies (Savage and Weinman, 1975; Wilheit et al., 1977). As in the nonprecipitating case, the 53.74-GHz channel continues to decrease monotonically with increasing liquid water. The larger effect of precipitation on the 53.74-GHz channel prevents its direct use (i.e., temperature determination) even in midlatitudes. However, it appears that this channel may be used to estimate precipitation with less ambiguity than the double-valued response at 50.30 GHz, particularly in the tropics where temperature variations are minimal. Also, although not explicitly shown here, land within the instrument's field of view can obscure the liquid water effect at 50.30 GHz; i.e., the increased emissivity can produce a similar increase in brightness temperature to that of liquid water. Since the 53.74-GHz channel is not significantly affected by the surface, it is less restricted than the more transparent channel.

In summary, these simulations show that both the 50.30- and 53.74-GHz channels provide liquid water information over the oceans. The use of the latter channel presupposes that temperature changes are negligible compared to the liquid water effects, a condition generally met in the tropics. The small amounts of liquid water (< 1 mm) generally associated with nonprecipitating clouds are best detected using the 50.30-GHz measurements. However, this channel becomes less sensitive for larger amounts of liquid water. Also, any land within the instrument's field of view can obscure the liquid water signature for this channel. The 53.74-GHz channel can provide a better estimate under these situations. Finally, the 54.96- and 57.95-GHz channels show negligible effects, even for precipitating clouds, and can therefore be used to provide temperature information.

2.2.3 Liquid water effects (measured)

Before beginning with a detailed study of Hurricane David, it is appropriate to conclude this section with an illustration of the above-mentioned channel characteristics using a sample of MSU measurements. A distinction will also be made between the temperature and liquid water effects for the lower sounding channel.

---

[2] Grody, N.C., 1979: Liquid water determinations over the oceans from MSU measurements. Memo for the record, 3 pp.

Figure 4 shows the 11 μ infrared images of Hurricane David for the four time periods of interest in this study. The measurements considered here correspond to the earliest time, September 3, at 0900 GMT, when David was in the Florida Strait as shown in the upper left image. For this discussion, only the measurements at the 9.5° scan position are used. As indicated by the dashed line on the infrared image, these observations pass over Cuba and almost directly over the hurricane center. The brightness temperatures are plotted in figure 5 and have been limb corrected and normalized to unity emissivity (only sounding channels) using the procedure outlined earlier.

The 50.30-GHz measurements increase from 228 K over the clear ocean (figure 4) reaching a peak value of 262 K near the hurricane center. However, in addition to liquid water, the influence of land within the field of view cannot be discounted for contributing some of the increase in the brightness temperature near the hurricane between 25 to 27 N (Florida Strait). Note a similar increase in brightness temperature near Cuba and the North Carolina coast, where horizontal averaging by the instrument reduced the 295 K expected value to the 265 K observations. As anticipated, no such emissivity effect is observed for the 53.74-GHz measurements; i.e., the maximum perturbation due to land was computed earlier to be less than 2 K, where a large part of this is removed by the emissivity correction procedure. Since this investigation examines the hurricane during its path along the East Coast (figure 4), the 50.30-GHz measurements cannot readily be used because of the distortion introduced by land effects. Only the 53.74-GHz channel will be considered for providing precipitation information over both land and sea surfaces.

In applying the 53.74-GHz measurements to monitor precipitation, it is necessary to correct for temperature effects when they become comparable to the effects of liquid water. Although this is not normally a problem for tropical atmospheres, there are larger temperature changes in the case of hurricanes which must be accounted for. Fortunately, an estimate of the temperature contribution is available from 54.96-GHz measurements which show an increase in brightness temperature near the hurricane center in figure 5. As discussed later, this real temperature contribution is also contained in the lower sounding channel along with the liquid water effect. As an approximation, the increase in the 54.96-GHz brightness temperature relative to the unperturbed state (designated by the base line) is subtracted from the 53.74-GHz measurements to obtain the effect of liquid water alone (temperature adjusted plot in figure 5). A more extensive examination of liquid water effects at 53.74 GHz will be presented in the detailed study to follow.

For completeness, the 57.95-GHz measurements are also displayed in figure 5. These data show no apparent hurricane influence, and, as discussed later, most of the variation in this channel occurs from changes in the tropopause height with latitude.

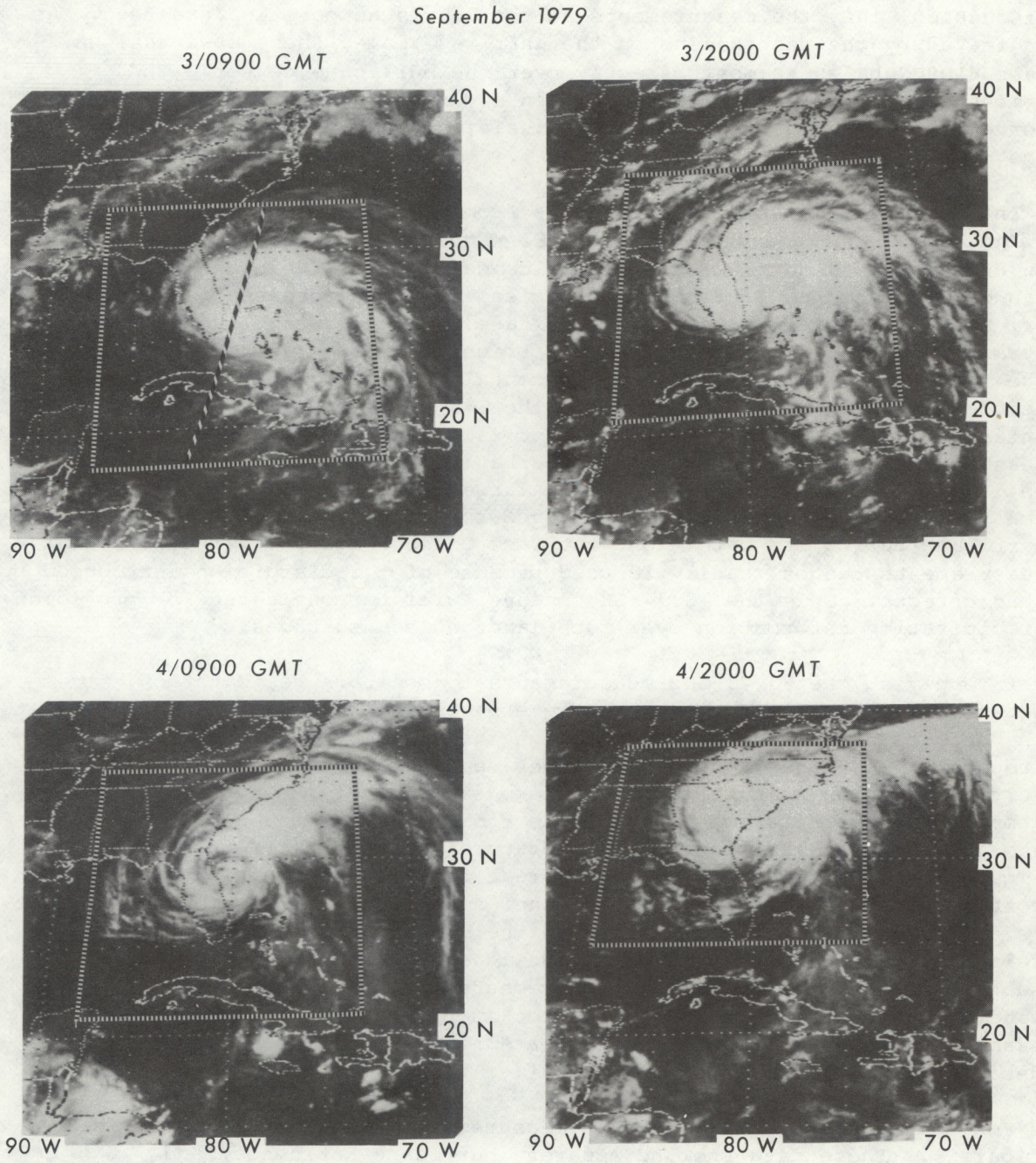

Figure 4. TIROS-N scanning radiomenter (11 μ) images of Hurricane David for time periods of interest. Areas enclosed by striped lines correspond to MSU observations in other figures.

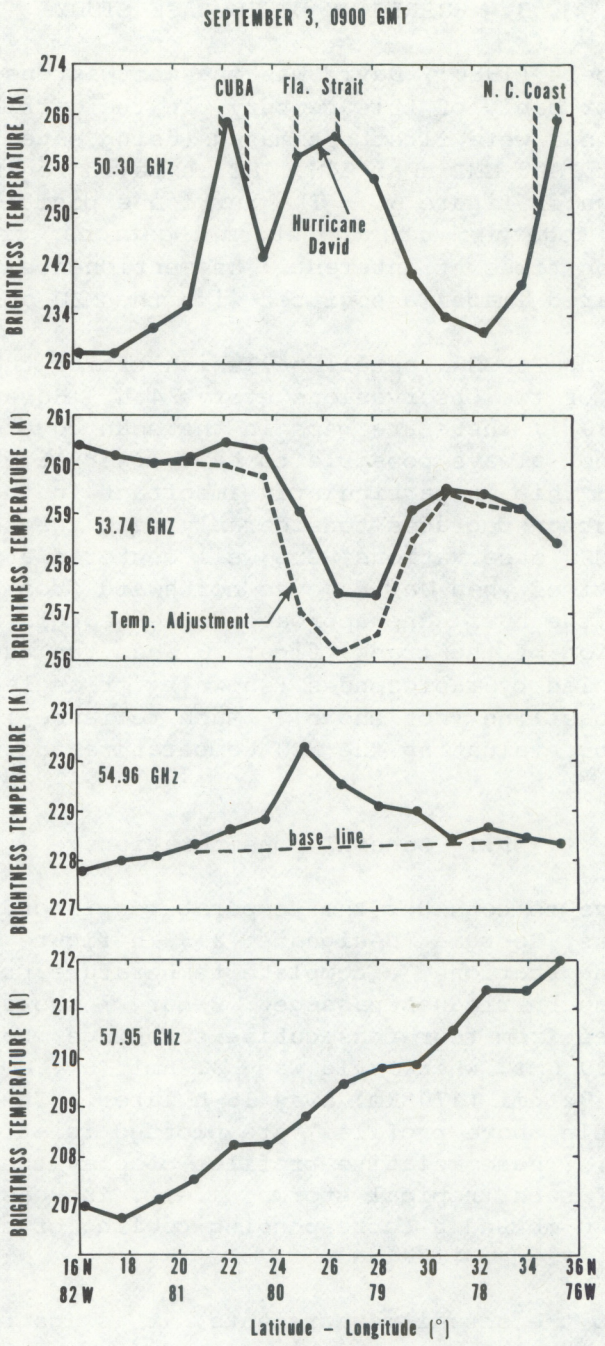

Figure 5. Cross section of brightness temperature measurements (limb corrected) passing through Hurricane David September 3, 0900 GMT. (See dashed line in figure 4.) The 50.30-GHz channel reponds to surface and cloud features. Temperature alone defines the 54.96- and 57.95-GHz measurements; the 54.96-GHz channel displays the hurricane's warm-core anomaly. Both precipitation and temperature affect the 53.74-GHz measurements; the "temperature adjustment" plot shows the response after removing temperature effects. (See text.)

3. HURRICANE DAVID CASE STUDY

As stated by Hebert (1980), David was the most intense hurricane of the 1979 season, and probably of this century, in the Carribean Sea area. Hurricane force winds were first estimated (using satellite images) on August 26 at about 1800 GMT near 24N, 48E as David began a parabolic track. (A section is shown in figure 6.) The hurricane position is shown every 12 h along the track together with the storm locations corresponding to the MSU observation times of interest. As mentioned earlier, figure 4 displays the infrared images associated with the MSU observations.

The polar orbiting TIROS-N satellite, which orbits the Earth twice daily, enables a maximum of two observations every 24 h. However, for low latitudes (below 30^{o}), there are gaps in the scan coverage for adjacent orbits and it is not always possible to have observations near the center of the MSU swath. This is particularly important in the case of hurricanes because the resolution degrades considerably near the scan edges (figure 1). Fortunately, the MSU observations were well centered at four consecutive 12 h observation times when David moved northward from near the Bahamas on September 3 until the hurricane approached the Georgia coast about 36 h later. This portion of the track (figure 6) has the additional advantage of being well sampled by radiosondes (shown by triangles) as well as by radar along the coastline (not shown). Much reliance is placed on the radiosonde data for evaluating the MSU temperature and wind related measurements.

3.1 General Considerations

It is informative to consider the temperatures recorded by the radiosonde station in Waycross, Georgia (designated 213 in figure 6). Unlike some of the other reporting stations, a complete temperature profile (to 30 mb) was obtained during the hurricanes passage. Figure 7 shows the "relative" profiles determined from four consecutive soundings, beginning on September 3 at 1200 GMT, when David was 332 nmi (614 km) from the station, until it was only 92 nmi (170 km) away 36 h later. The three closest soundings (See table above profiles) are plotted relative to that of the earliest sounding. These relative profiles display the unique characteristics of such tropical storms, i.e... increased warming towards the center near 300 mb and a corresponding cooling of smaller magnitude near 100 mb (e.g., Frank, 1977).

Before examining the actual measurements, it is instructive to compare the clear-column brightness temperatures computed for the 53.74-, 54.96-, and 57.95-GHz channels (at nadir and unity emissivity) using eq. (1). Integrating the three relative profiles by the weighting functions (shown opposite the profiles) results in the brightness temperature changes tabulated in figure 7. The tabulated results show that the warm core anomaly near 300 mb (7.4 K maximum on September 5) is reduced by more than 60 percent by the weighting functions of both the lowest and middle peaking channels. However, as indicated in figure 3 and demonstrated in

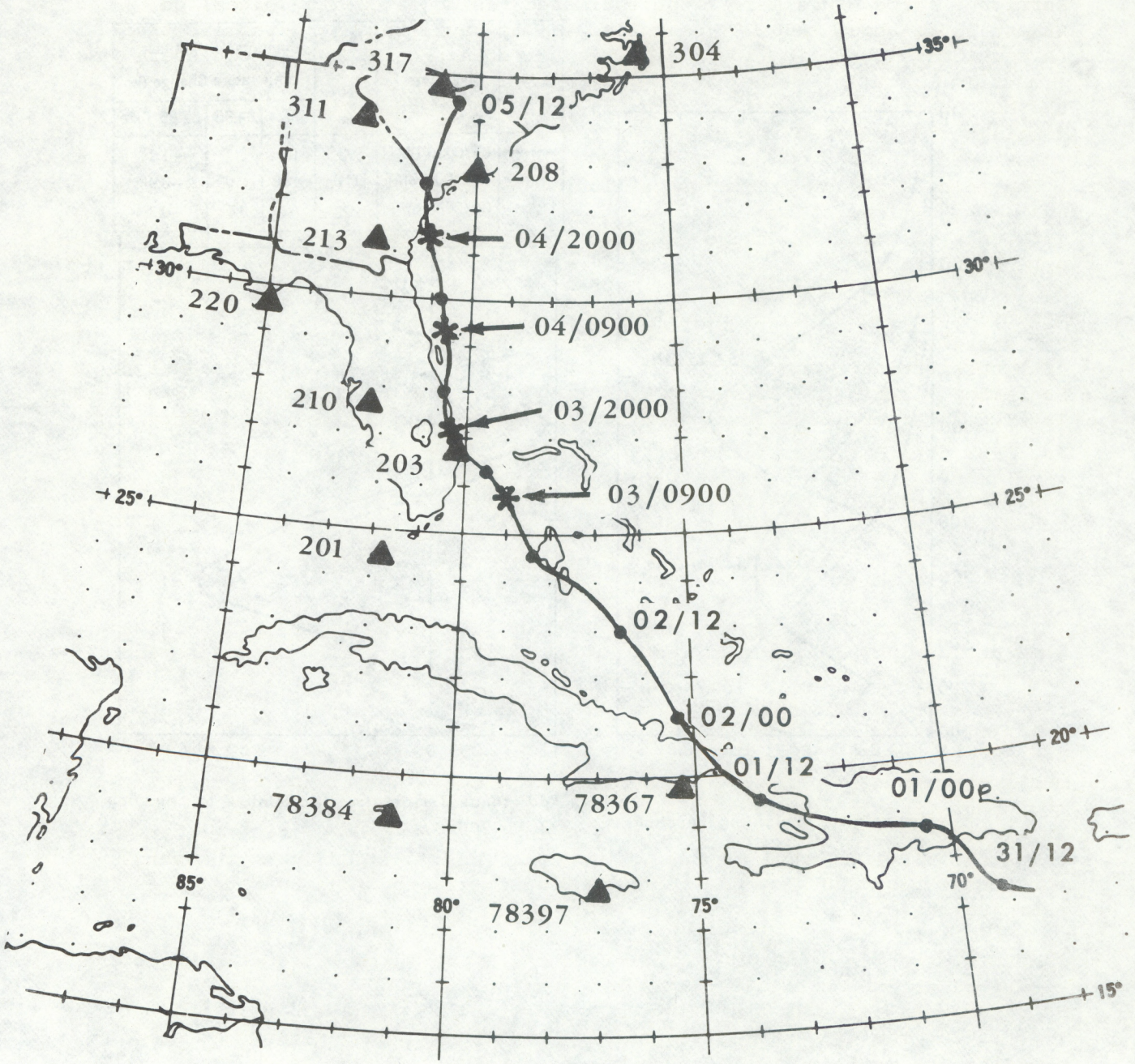

Figure 6. Hurricane David track showing positions at synoptic times (dots) and MSU observation periods of interest (asterisks). Radiosondes are located at triangles and referred to by station number.

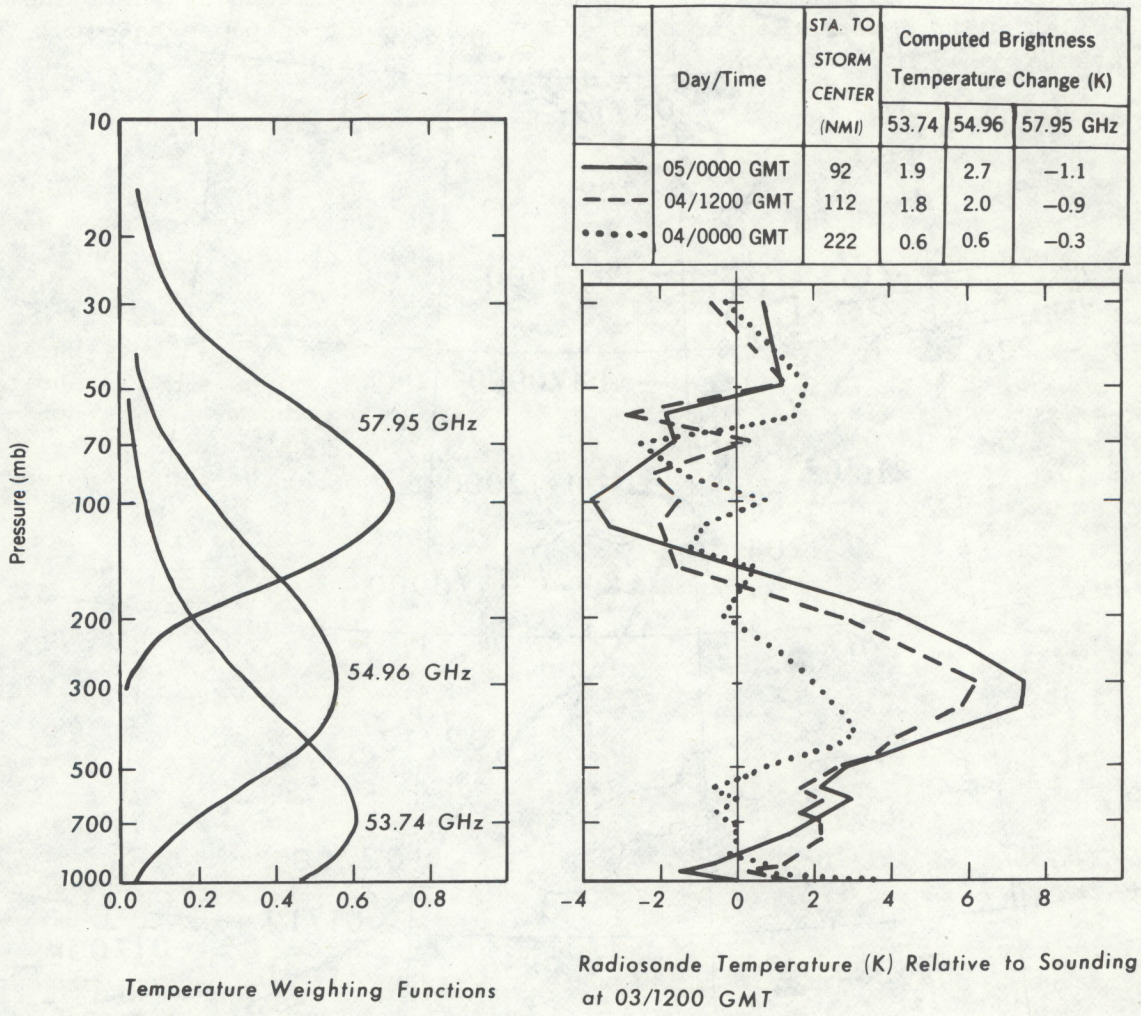

Figure 7. Radiosonde temperature profiles (right) at three consecutive times in Waycross, Georgia (Sta. 213), relative to sounding on September 3, 1200 GMT. Temperature weighting functions at nadir for unit emissivity surface are shown for reference (left). Table indicates radiosonde times, distance from hurricane, and change in computed brightness temperature based on the three "relative" profiles.

figure 5, liquid water effects can exceed the relatively small change due to temperature for the 53.74-GHz channel without appreciably affecting the 54.96-GHz clear-column values. Also observe from the table that the 57.95-GHz channel responds to the even smaller temperature change (negative) near 100 mb where this channel peaks. This perturbation due to the hurricane is not obvious from the measurements of figure 5, where the larger latitudinal variation arising from changes in tropopause height appears to dominate.

3.2 Brightness Temperature Measurements

Figures 8 through 11 display the MSU brightness temperature measurements as well as the available conventional data to be used for comparison. Each figure corresponds to a different observing time and displays the contoured brightness temperatures (0.5 K interval) for the three sounding channels along with a radar summary map. The radar summary map is prepared routinely by the National Weather Service by compositing the various radar data on conventional map projections with the level-1, -3, and -5 intensity contours shown. As mentioned before, the 50.30-GHz measurements are not considered in this study since much of the important area under investigation lies near coastal boundaries which obscure the liquid water signature for this channel.

All brightness temperature maps were produced by hand-analyzing the individual measurements after they were normalized to nadir and unity emissivity. As shown in figure 8, the individual maps also contain the computed clear-column brightness temperatures (solid dots) obtained, as before, by integrating the radiosonde profiles over the corresponding weighting functions. Only those soundings which extend to at least 30 mb are used in the computations for the two highest peaking channels. Beyond this cutoff level, the profiles are extended to 1 mb based on time interpolated radiosonde data and climatological insertions. This cutoff restriction is relaxed to 100 mb for the 53.74-GHz channel, so that one generally finds more radiosonde computed values for this channel than for the other two. These radiosonde values are repositioned from their station locations to approximately account for the hurricane movement during the time between the MSU and radiosonde observations (fig. 6). The brightness temperature maps in figures 8 through 11 are compared with the inserted radiosonde values to examine the microwave measurements.

The 54.96- and 57.95-GHz maps (figs. 8-11) also display the radiosonde measured winds at 700 and 50 mb, respectively. The directions of these winds will be compared with the isotherm pattern for the two channels. Because of the difficulty of obtaining upper air measurements near the hurricane, there are more 700 mb winds displayed than 50 mb winds. Also, for reference, the individual MSU observation points are indicated as open circles on the 53.74-GHz maps, while the 54.96-GHz maps contain a straight dashed line to represent the nadir viewing positions.

To aid in the comparison between the measured and computed brightness temperatures, a time series was prepared of the data sets for the 54.96-and 57.95-GHz channels. These plots are shown in figure 12 for the radiosondes which lie along the hurricane track (fig. 6) and will be referred to when discussing these two channels. Since only a limited number of radiosonde values are available, there are more measurements shown (solid line) than computed values (dashed line). The two sets of observations are displayed at their respective observation times with the measurements interpolated to the actual radiosonde locations. In plotting the measurements, corrections are made for the biases observed later (section 3.3) relative to the computed values.

3.2.1 September 3, 0900 GMT

Figure 8 shows the results for the earliest observation time, when David was off the Florida coast (fig. 4) with about a 974 mb central pressure and deepening (Hebert, 1980). To be consistent, all four dates will be analyzed beginning with the lowest sounding channel, followed by the next highest channel, etc. Subsequently, a data summary will be presented for the complete study period. (The time series shown in figure 12 was prepared as part of that summary.)

The 53.74-GHz measurements in figure 8 agree well with the eight computed brightness temperatures (indicated near the solid dots), both having values near 260 K and decreasing with increasing latitude. From the statistical summary presented later, little difference is found between the measured and computed values for all the nonprecipitating cases. There is, however, a colder region north of the hurricane center which is suggestive of precipitation effects. (The center is obtained from figure 6 and indicated by the $\mathcal{S}$ symbol.) Since radiosonde data are not available for comparison at this time, this feature is examined by referring to the radar summary map. To aid in the radar comparison, the 257 and 258 K contours are superimposed on the radar map. This form of comparison with radar data will be continued for the other time periods. Note that the smaller 257 K contour intersects the level-3 radar intensity contour, although the land-based radar begins to cut off where the larger 257 K contour exists. There is however a distinct separation between the level-3 intensity region surrounding the hurricane center and the larger 257 K contour. This suggests that the effect of liquid water attenuation may, in part, be compensated for by the actual temperature increase near the center.

The temperature effect can be approximately removed using the procedure outlined earlier (figure 5) which employs the 54.96-GHz measurements. From the 54.96-GHz map, it is observed that the 228 K outer contour, which approximates the background level, extends to about a 5° radius from the center, while the maximum contour of 230 K has only about a 0.5° radius. This 2 K difference around the center between the maximum anomaly and the background is partly contained in the 53.74-GHz measurements. Subtracting out this warm-core anomaly results in a 2 K further reduction of the contour values within about 0.5° radius of the hurricane center.

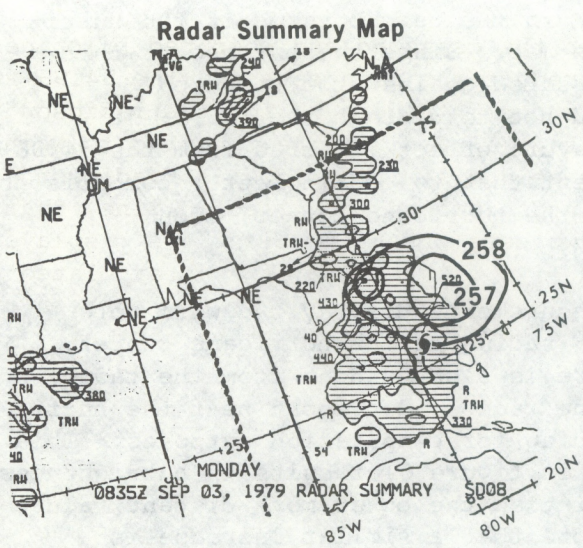

Radar Summary Contours at Intensities 1 - 3 - 5
Cloud Tops in 100s of ft.

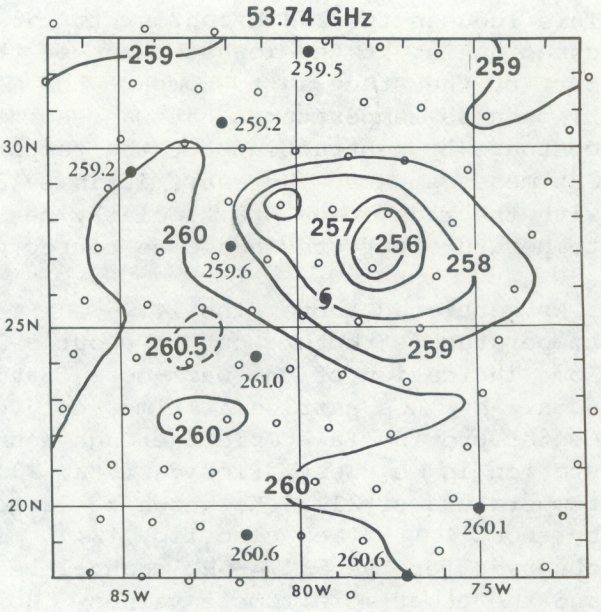

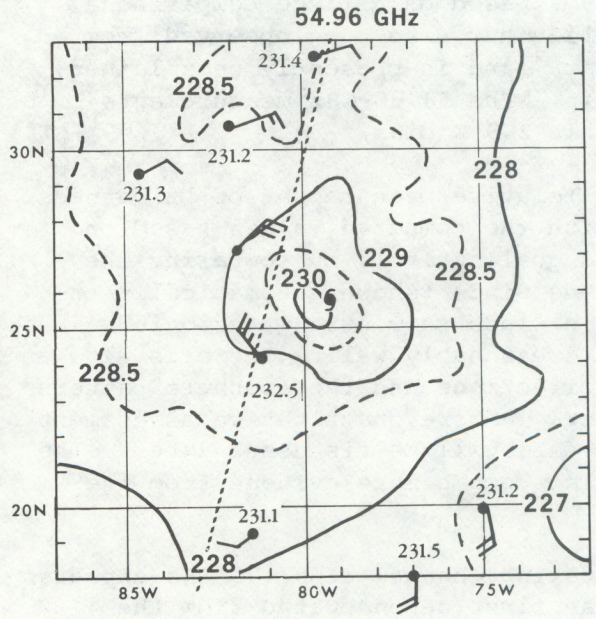

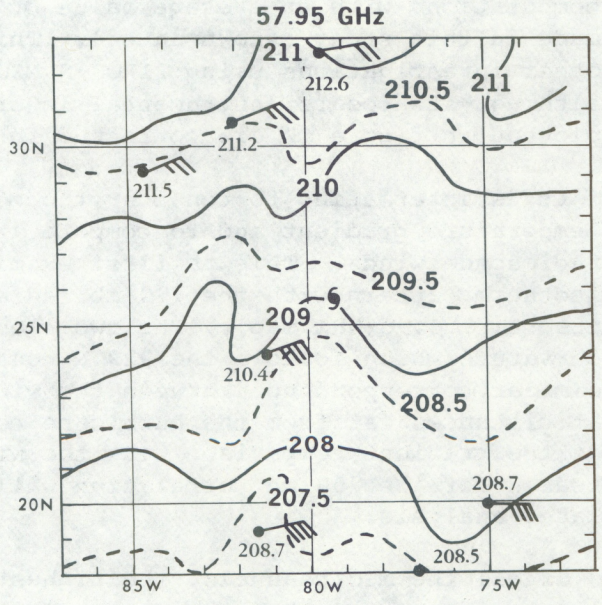

Figure 8. Brightness temperature measurements (limb corrected) for September 3, 0900 GMT, compared with radar data at 0835 GMT and radiosonde data at 1200 GMT. Radar summary chart (upper left) with superimposed 53.75-GHz contours at 257 K and 258 K. The 53.74-GHz contour map (upper right) contains radiosonde computed values (dots) and MSU observation points (open circles). The 54.96-GHz map (lower left) contains radiosonde values and radiosonde winds at 700 mb (full barbs = 10 kn); the straight dashed line indicates MSU nadir viewing positions. The 57.95-GHz map (lower right) contains radiosonde values and 50 mb radiosonde winds.

This reduces the 258 K contour to 256 K in the neighborhood of the hurricane, making it the lowest value on the map. Since the purpose of this part of the study is to compare the measured against the computed brightness temperatures, it was decided not to distort the 53.74-GHz contours by subtracting out the temperature effect inferred from the 54.96-GHz measurements. However, it is evident that to obtain better comparisons with the radar data, particularly near the hurricane center, such temperature effects should be corrected.

As mentioned above, the 54.96-GHz measurements display the warm core temperature structure out to about a 5^{o} radius of the hurricane center. Some indication of the warm-core feature is also evident from the radiosonde data. At this particular time, only one radiosonde report near the hurricane center provided a complete enough sounding for computation purposes. This station in Key West, Florida (Sta. 201 in figure 6) results in a brightness temperature of 232.5 K, which is larger than the other more distant values by about 1 K. (See also fig. 12.) Note that a similar increase is observed for the 53.74-GHz channel between its radiosonde value of 261.0 K and the other more remote values. However, in the case of the 54.96-GHz observations, there is a disparity between the measured and computed brightness temperatures. Everywhere, the measurements are lower than the computations with an average value of 2.9 K based on all the comparisons made in this study (shown later). This bias has also been observed from other investigations using TIROS-N MSU data[3] and is presently unexplained, although it appears instrumental in origin. The 54.96-GHz measurements plotted in figure 12 are corrected for this 2.9 K bias.

It is interesting to consider the more relative measurement of brightness temperature gradient and to compare it with the computed values based on radiosonde winds. This is first examined qualitatively by comparing the isotherm pattern with the 700 mb radiosonde winds (shown schematically on the same 54.96-GHz map). The two close-in winds show strong cyclonic curvature which follows the 229 K contour reasonably well. There is also a similar correspondence between the wind directions and the isotherm pattern at distances far from the hurricane center. A more quantitative assessment of the gradient comparison with the wind data will be discussed later. The reason for the 700 mb correlation will also become more evident from the later analysis.

Of all the MSU channels, the highest peaking channel at 57.95 GHz appears least affected by the hurricane. This was first demonstrated from the sample measurements in figure 5 and then by the introductory computations of this section. It is therefore not surprising to find only minor variations in the contours around the hurricane center. Of all the contours, the 208.5 K value shows the largest variation and will be examined further at the next observation period. Compared with the radiosonde values, the 57.95-GHz measurements display a similar increase in brightness temperature with increasing latitude. However, the measurements are lower everywhere compared to the computed values. From the complete set of radiosonde comparisons presented later, a bias of 0.6 K is determined, where the measurements shown in figure 12 are corrected for this bias. However, in addition to the bias, the 57.95-GHz measurements are later found to be more variable relative to the radiosonde data than the 54.96-GHz results.

[3] Grody, N.C., 1979: MSU Calibration. Memo for the record, 4 pp.

By comparing the isotherm pattern at 57.95 GHz with the winds at different pressure levels, it is generally found that the best correlation occurs for the 50-mb level. A sample of such comparative data is given later together with a discussion on the wind and gradient relationship for this channel. This correspondence between the wind directions at 50 mb and the isotherm pattern is shown here by referring to the 57.95-GHz map. The radiosonde winds at 50 mb are plotted schematically and follow the isotherm pattern quite well throughout the map.

3.2.2 September 3, 2000 GMT

As evident from Figures 4 and 6, David struck the Florida coast, just north of Palm Beach at about this time, with a central pressure decreasing to about 972 mb. The brightness temperature fields are displayed in figure 9 along with the radiosonde data and a radar summary map for comparison.

At this time, seven radiosondes had obtained a complete enough sounding for computing the 53.74-GHz brightness temperatures within about a 7^{o} radius of the hurricane. Three of them are positioned around the 259 K contour which surrounds the hurricane (Sta. 210, 213, 208) and are particularly useful for examining the channel measurements. Observe that all three values are greater than the 259 K contour value, with the largest difference being nearly 2 K at Tampa, Florida (Sta. 210). The other two radiosondes are farther from the hurricane and are only about 1 K larger than the measurements. These differences arise mainly due too precipitation within the field of view which lowers the brightness temperature measurements. The larger difference observed in Tampa, Florida probably occurs beceause of more extensive precipitation within the viewing area. As before, the region with contour values less than 259 K is too remote for comparison with radiosonde data and must be examined qualitatively using radar information.

The lowest contour values of 257 and 258 K (above the hurricane center) are rotated counterclockwise relative to the previous case. This agrees with the change in the level-3 radar contour west of the hurricane which also displays a similar rotation at this time. It is once more found that the larger 257 K contour, located farther east, extends beyond the radar range. Also, temperature effects must again be accounted for near the center of the hurricane. This would explain the larger brightness temperature measurements near the center (258 K) and the reason for separation of the 257 K contour from the level-3 radar contour surrounding the hurricane center.

A second region containing 257 and 258 K contours exists in the upper left corner of the 53.74-GHz map. This area is identified by a bright cloud pattern in the infrared image (fig. 4) and by a line of radar echos beginning around the northwest section of Georgia. Although the lower contour value of 257 K is evidently due to precipitation, the channel also responds to the colder temperatures accompanying the convective system. This is supported by the close comparison between the 258.6 K radiosonde value in Athens, Georgia (Sta. 311) which lies on the 259 K contour.

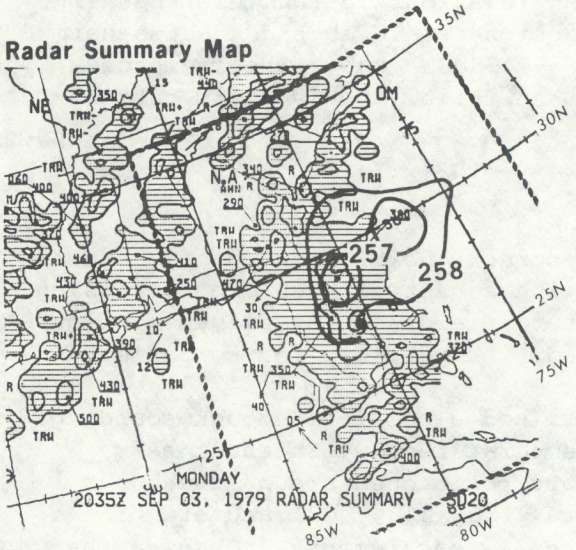

Radar Summary Contours at Intensities 1 - 3 - 5
Cloud Tops in 100s of ft.

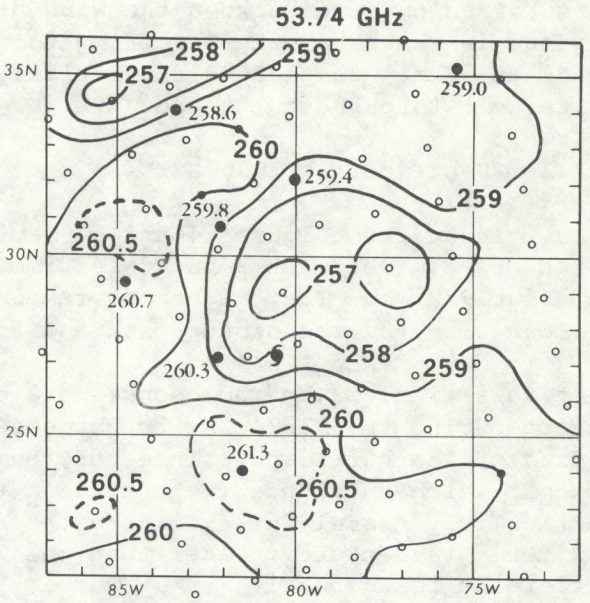

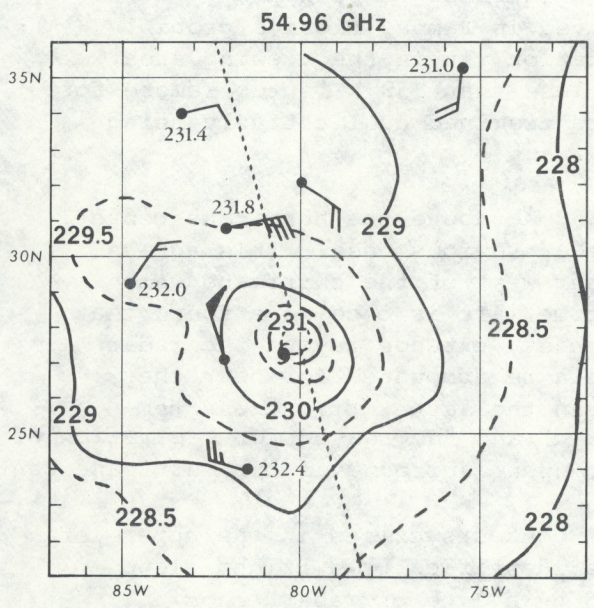

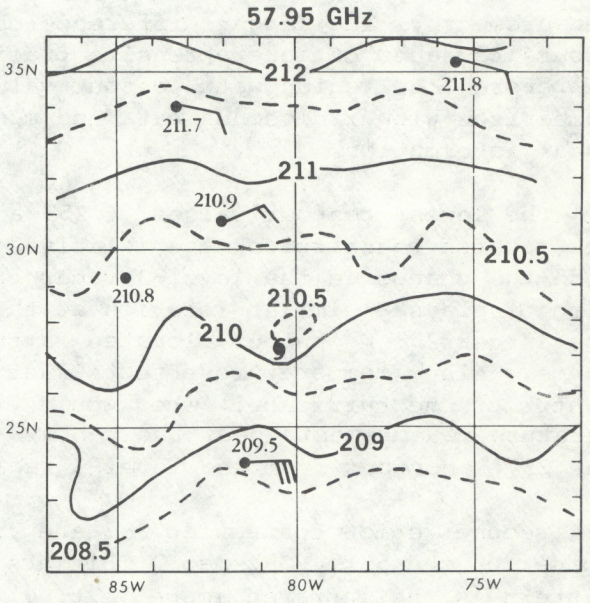

Figure 9. As in figure 8 except for MSU measurements on September 3, 2000 GMT. Radar data at 2035 GMT, radiosonde data on September 4, 0000 GMT.

The two highest contour values of 260.5 K are in the clearer areas northwest and south of the hurricane (figure 4). These contour values are larger than the 260 K background level and are examples of brightness temperature measurements responding to the warm-core temperature structure of the hurricane. This is evident from the comparisons with the 54.96-GHz measurements that reveal the horizontal extent of the warm-core structure throughout the hurricane. Both areas containing these 260.5 K contours are within the warm-core region (approximately defined by the size of the 229 K contour at 54.96 GHz) and are comparable with the neighboring radiosonde values.

Comparing the 54.96-GHz maps in figures 8 and 9, we observe a 1.5 K increase in the maximum contour value (from 230 K to 231.5 K). Compared to the previous time, the 230 K contour has also expanded in size from a 0.5° radius to about a 1.5° radius. This suggested increase in hurricane intensity is partly supported by the 2 mb decrease in central pressure reported about this time. Also, the three radiosondes positioned around the 229.5 K contour have values greater than or equal to the earlier results. The radiosonde values in Waycross, Georgia (Sta. 213) and Appalachicola, Florida (Sta. 220) are both about 0.7 K larger than the previous values and agree with the change in the contour values near the stations as well as the measurements shown in figure 12. The radiosonde in Key West, Florida (Sta. 201) reports no significant change in the computed values at the two times and also agrees with the measurements displayed in figure 12 as well as with the different contour maps.

Although the three radiosondes around the hurricane compare reasonably well with the measurements, figure 12 shows a large difference at this time in Athens, Georgia. Compared to the earlier time, the 54.96-GHz measurements are about 0.5 K warmer while the radiosonde value is almost unchanged. As mentioned above, this region contains convective elements which, because of their dynamic characteristics, can lead to large temperature differences over the 4-h period between the MSU and radiosonde observations. As we shall see, the differences are less between the two types of observations at later times when the system has dissipated.

As discussed before, the 700 mb winds also reflect the pattern of the 54.96-GHz measurements. All wind observations within the 229 K contour display the cyclonic circulation of the hurricane and follow the isotherm pattern. It is consistently found throughout this study that the 700 mb wind directions are an excellent indicator of the brightness temperature pattern, especially those contours having values less than or equal to 229 K.

The 57.95-GHz measurements are not as consistent with the radiosonde values as are the lower sounding channels. In particular, the computed brightness temperature at Key West, Florida (Sta. 201) is 0.9 K lower than the previous time, although the contour value remains close to 209 K at both times. This disparity is also noted in figure 12 which shows a much larger change for the radiosonde values in Key West, Florida than in the corresponding measurements. However, unlike the measurements, the change in the radiosonde value is also seen to be much larger than that computed for the 54.96-GHz channel. It appears unlikely that the stratospheric channel should exceed the variations of the tropospheric channel. (For example see figure 7).

As such, this vertical inconsistency is possibly due to radiosonde errors in the stratospheric measurements. One can also anticipate greater mismatch between the MSU measurements and radiosonde data in the stratosphere due to a slant in the radiosonde trajectory and the 4-h time difference between the two types of measurements. Further studies must be conducted to better isolate the source of this disparity.

Compared to the previous time, the variations in the isotherm pattern at 57.95 GHz now extends northward to the 210 K contour. There is also an increase in brightness temperature near the hurricane center, suggesting a possible expansion in the vertical as well as horizontal structure of the warm core. As before, the isotherm pattern follows the 50 mb winds at all latitudes.

3.2.3 September 4, 0900 GMT

Hurricane David has now moved slightly off the Florida coast (fig. 6) with about a 1 mb drop in central pressure to 971 mb. Also, the infrared image in figure 4 shows an open eye with less cirrus coverage than previously. Figure 10 contains the results for this time period and will be compared with the earlier observations.

Compared with the 53.74-GHz maps shown in figures 8 and 9, there appears to be a merging of the two 257 K contours into an elongated distribution that is further rotated counterclockwise. The 257 and 258 K contours which bound this distribution are reproduced as before on the radar map for comparison. In general, the 258 K contour encloses the level-3 radar contour north of the hurricane, while the 257 K contour lies mainly within the level-3 intensity region. However, at this time, a level-5 contour is also observed and coincides with the lowest brightness temperature contour of 255 K. This 255 K contour is the lowest value found during the complete study and occurs just off the Carolina coast below the Charleston radiosonde station (Sta. 208). In fact, this station did not report a sounding above 400 mb, so that brightness temperatures could not be computed for any channel. More complete soundings were obtained in the less active areas.

The clearer area west of the hurricane (fig. 4) contains the largest contour value of 261 K. Surrounding this contour is a 260.5 K contour which actually goes around the hurricane center and agrees to within 0.5 K with the radiosonde value located on this contour. As evident from the 54.96-GHz map, those contour values larger than 260 K are a response of the 53.74-GHz channel to the hurricane's warm-core structure. The other 260.5 K contour located south of the hurricane also agrees closely with the radiosonde value of 260.7 K shown. This clear region is farther from the hurricane center and indicates a smaller perturbation due to the hurricane, consistent with the reduction of the warm-core temperature shown by the 54.96-GHz map. Also, the brightness temperature around the center is greater than the 259 K value found previously, suggesting less liquid water than in the other two cases. This is supported by the infrared image which shows less cloud coverage on the western side of the hurricane compared to the other images.

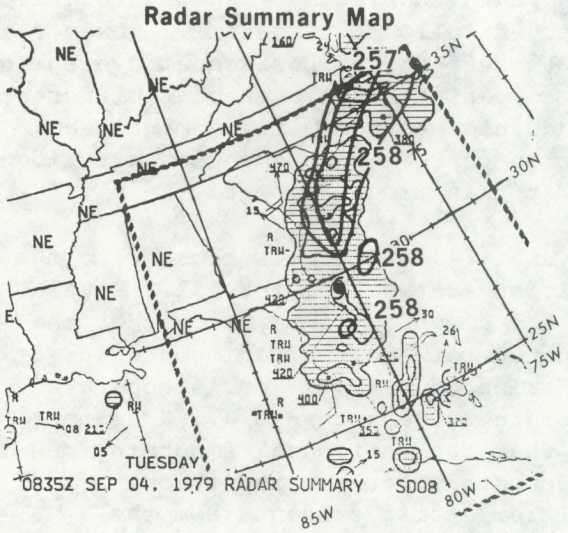

Radar Summary Contours at Intensities 1 - 3 - 5
Cloud Tops in 100s of ft.

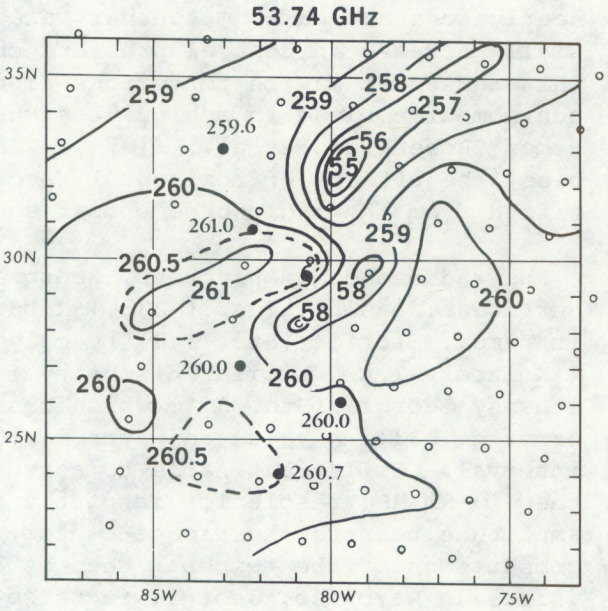

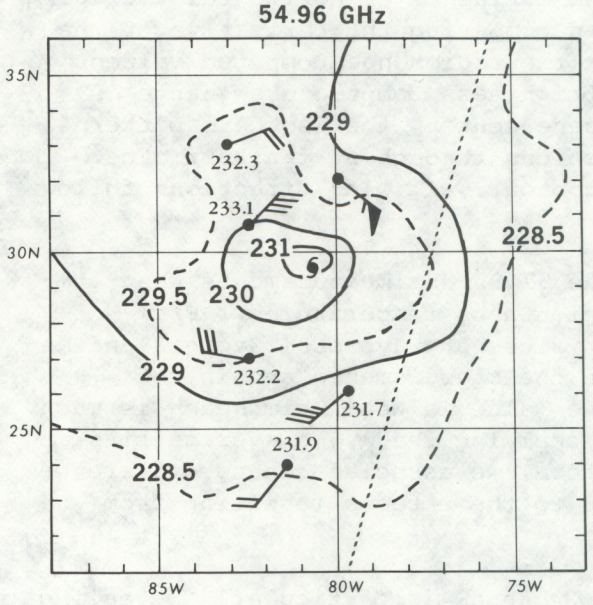

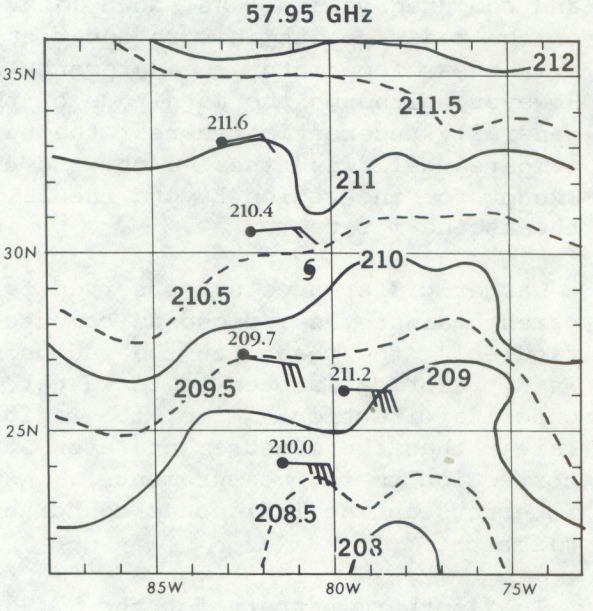

Figure 10. As in figure 8 except for MSU measurements on September 4, 0900 GMT. Radar data at 0835 GMT, radiosonde data at 1200 GMT.

At 54.96 GHz, the measurements close to the hurricane center have similar appearance to that of the previous time. There is only a 0.5 K decrease in the maximum contour value (from 231.5 to 231 K) and no substantial decrease in the size of the 230 K contour. A more quantitative measure of the brightness temperature pattern is given by the radial derivative of the brightness temperature and will be presented later for comparison. The nearly constant maximum contour value appears consistent with the relatively small decrease in central pressure observed following landfall. However, this agreement may be fortuitous since the effects of horizontal averaging can sometimes lead to ambiguities when comparing measurements at different times (Rosenkranz et al., 1978). In addition to the already mentioned bias, the effects of horizontal resolution on the measurements can be identified from the radiosonde comparisons at this time.

The radiosonde in Waycross, Georgia (Sta. 213), which is closest to the hurricane, has a value of 233.1 K but is separated from the 232.2 K value in Tampa, Florida (Sta. 210) by only a 0.5 K contour interval rather than a 1 K interval. A similar disparity is noted between the radiosonde in Athens, Georgia (Sta. 311) which has a value of 232.3 K and is separated from the 233.1 K value in Waycross, Georgia by less than a 0.5 K contour interval. It is reasonable to asssume that the horizontal smoothing due to the 110-km MSU resolution is partly responsible for the reduction in amplitude near the hurricane center. This is also evident from the comparisons of the temporal changes shown in figure 12. The radiosonde values in Waycross, Georgia increase more than the measurements. No such comparison can be made between the changes observed in Athens, Georgia because of the inconsistency found at the earlier time between the measured and computed values. As shown later, the influence of horizontal averaging on the measurements is more apparent when comparing the derivative of the brightness temperature measurements with the radiosonde computed values. However, although the magnitude of the brightness temperature change is generally underestimated near the hurricane center, the isotherm pattern compares well with the 700 mb wind directions throughout the hurricane. Except for the region beyond the 229 K contour, all wind directions follow the isotherm pattern.

Larger differences are observed for the 57.95-GHz measurements when compared against the radiosonde computed brightness temperatures. From figure 12, the change in the radiosonde values at Waycross, Georgia and Key West, Florida is seen to be larger than the measurements and in the opposite direction. Also, the radiosonde value in West Palm Beach is much larger than the measurement (even after applying the 0.6 K average bias correction to the measurements). As before, we associate these differences to errors in the radiosonde sounding and to the effects resulting from mismatch.

The isotherm pattern for the 57.95-GHz channel is particularly revealing at this time. Due to the northward movement of the hurricane, we now observe variations in the 210.5 K contour as well as the lower contour values observed previously. However, unlike the small perturbations found earlier, a large-amplitude longitudinal wave is observed in the contour variation. This is barely evident from the 210 K contour at the previous time. As anticipated, the 50 mb radiosonde winds follow the isotherm pattern as before, although an insufficient number of observations are available to compare the wavelike pattern in the measurements.

3.2.4 September 4, 2000 GMT

This last set of data corresponds to the time when David approached the Georgia coast (figure 6) at Savannah Beach with a 1-mb decrease in central pressure to 970 mb. According to surface reports, the maximum winds remained at nearly 85 kn (42 m/s) from the time David left Florida until it approached Georgia (Hebert, 1980). However, as shown below, the brightness temperature measurements indicate an expansion of the warm-core structure as a result of possible orographic effects.

The 53.74-GHz measurements in figure 11 show a minimum contour value of 257 K compared to the 255 K minimum found previously. This, at first, appears inconsistent with the radar summary map since the level-5 radar intensity region is near the same location at both times. In fact, at this later time, the maximum intensity region is elongated farther northward and covers a larger area; a portion is unfortunately obscured by the "257" symbol on the radar map. This 2 K difference in the measured brightness temperature for the same radar intensity is explained by considering the effect of temperature on the measurements. Referring to the 54.96-GHz map, one observes an expansion of the 230 K contour to more than double the size of the previous time. This larger warm-core structure provides more temperature compensation for the effect of liquid water and thereby results in higher brightness temperatures than previously obtained. The radiosonde comparisons enable a more direct measure of precipitation effects. Note that there is a 2.8 K decrease in the 53.74-GHz brightness temperature at the northernmost position of the 257 K contour when compared with the radiosonde value of 259.8 K. This radiosonde report in Greensboro, North Carolina (Sta. 317) is just north of the maximum radar intensity contour (level-5). The 2.8 K difference is the largest reported in this study and is due to liquid water attenuation. Also, since the radiosonde values located between the 259 and 260 K contours are all more than 1 K larger than the measurements, these observations must contain the effect of liquid water. In contrast to these decreases in the brightness temperature measurements, an increase is shown in the clearer regions south of the hurricane (figure 4). The largest contour value of 261 K compares exactly with the radiosonde value on the contour. A similar observation is noted in the case of the two 260.5 K contours, where the differences between the measured and computed values are about 0.5 K.

As with the 54.96-GHz maps in figures 9 and 10, the maximum contour value deviates by $\pm$ 0.5 K from the 231 K average value. This appears to agree with the small changes in central pressure during the 24-h period, although, as mentioned before, the maximum anomaly measured by the MSU can also be affected by changes in the size of the eye region due to the horizonal averaging effect. The effect of horizontal averaging is once more evident by comparing the spatial variation of the measured and computed brightness temperatures around the hurricane center. Observe that the radiosonde in Waycross, Georgia (which is closest to the hurricane) has a 233.8 K value and is located on the 230.5 K contour, while the radiosonde in Athens, Georgia has a 232.8 K value but is, in fact, shown closer to the 231 K contour value. More evidence of the horizontal averaging effect will be presented later.

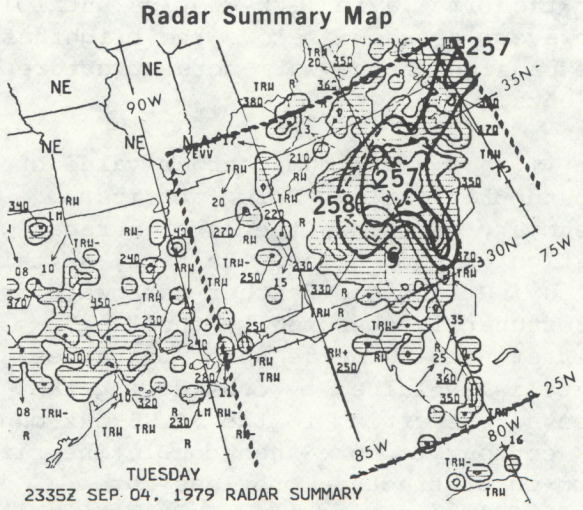

Radar Summary Contours at Intensities 1 - 3 - 5
Cloud Tops in 100s of ft.

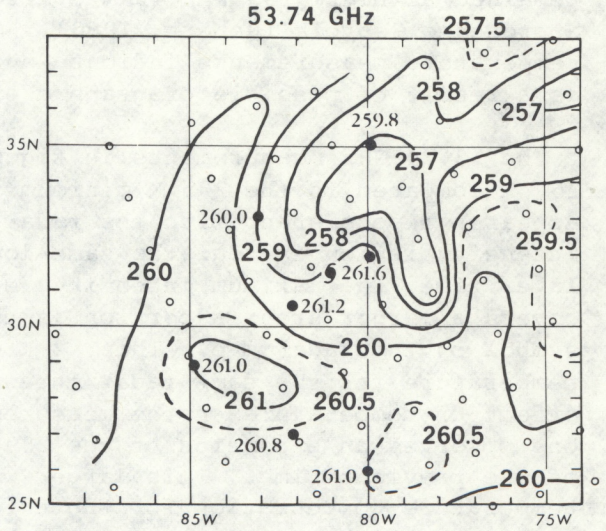

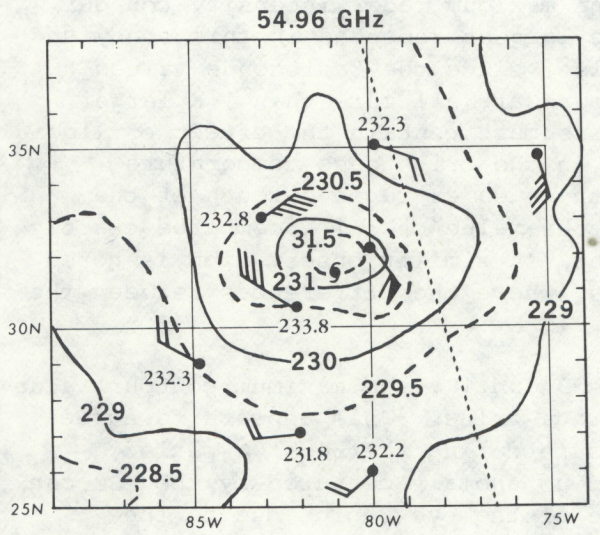

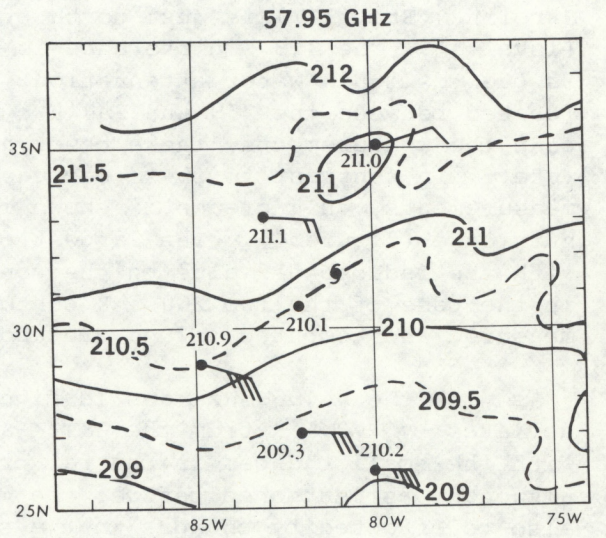

Figure 11. As in figure 8 except for MSU measurements on September 4, 2000 GMT. Radar data at 2335 GMT, radiosonde data on September 5, 0000 GMT.

The close correspondence between the 700 mb wind directions and the isotherm pattern helps to substantiate the extensive warm-core structure measured at this time. No such evidence from other conventional data exists, and no mention was made in the summary report (Hebert, 1980). One generally expects some dissipation of the hurricane as it tracks over land as a result of orographic effects. This is depicted by the expanded thermal pattern shown here.

Differences are again observed between the measured and computed values at 57.95 GHz. The differences are best identified by referring to figure 12 and by first comparing the radiosonde values against one another. It is apparent that the radiosonde value in West Palm Beach is larger than the values either north or south of the station. This same inconsistency in the latitudinal variation was noted earlier for this radiosonde station and again does not agree with the measurements (which show a continuous increase in brightness temperature with increasing latitude). The most striking difference in the temporal variations is that shown in Waycross, Georgia. Although both types of observations appear continuous in time, the measurements give no indication of a decrease for increasing time as in the case of the radiosonde data. It appears again that the radiosonde data in the stratosphere is not representative of the microwave measurements. Although it is difficult to single out a specific source of discrepancy, the radiosonde profiles for this station are, in fact, quite noisy in the stratosphere (figure 7). This is in contrast to the more uniform vertical structure observed in the troposphere. It may be argued that these temperature variations above 100 mb are "real", except that their corresponding horizontal scale is too small to be resolved by the MSU. As such, the negative changes in the computed brightness temperature are unresolved by the MSU measurements in figure 12.

With regard to the contour pattern, it is interesting to find a similar longitudinal wave as previously observed. From this and the earlier observations, it is evident that the variation in the contours propagates northwards with the hurricane movement. The 211 K contour displays the wave pattern, where it was earlier observed in the 210.5 K contour and possibly in the 210 K contour pattern at the second observing period. As for the other periods, no evidence of this pattern is found from the computed brightness temperatures or from the 50 mb radiosonde winds. The winds do, however, follow the isotherms reasonably well as before.

3.3 Summary of Brightness Temperature Comparisons with Radiosonde Data

Figure 13 summarizes the results of the previous case studies regarding the brightness temperature comparisons with radiosonde data. The brightness temperature mesurements for the three sounding channels are plotted on separate diagrams against the corresponding radiosonde (RAOB) computed values. As indicated by the table in figure 13, different symbols are used to distinguish the data obtained for the different times. Each scatter diagram shows the mean difference and standard error for the matchups with a solid line to represent perfect correlation and a dashed line to define the mean difference.

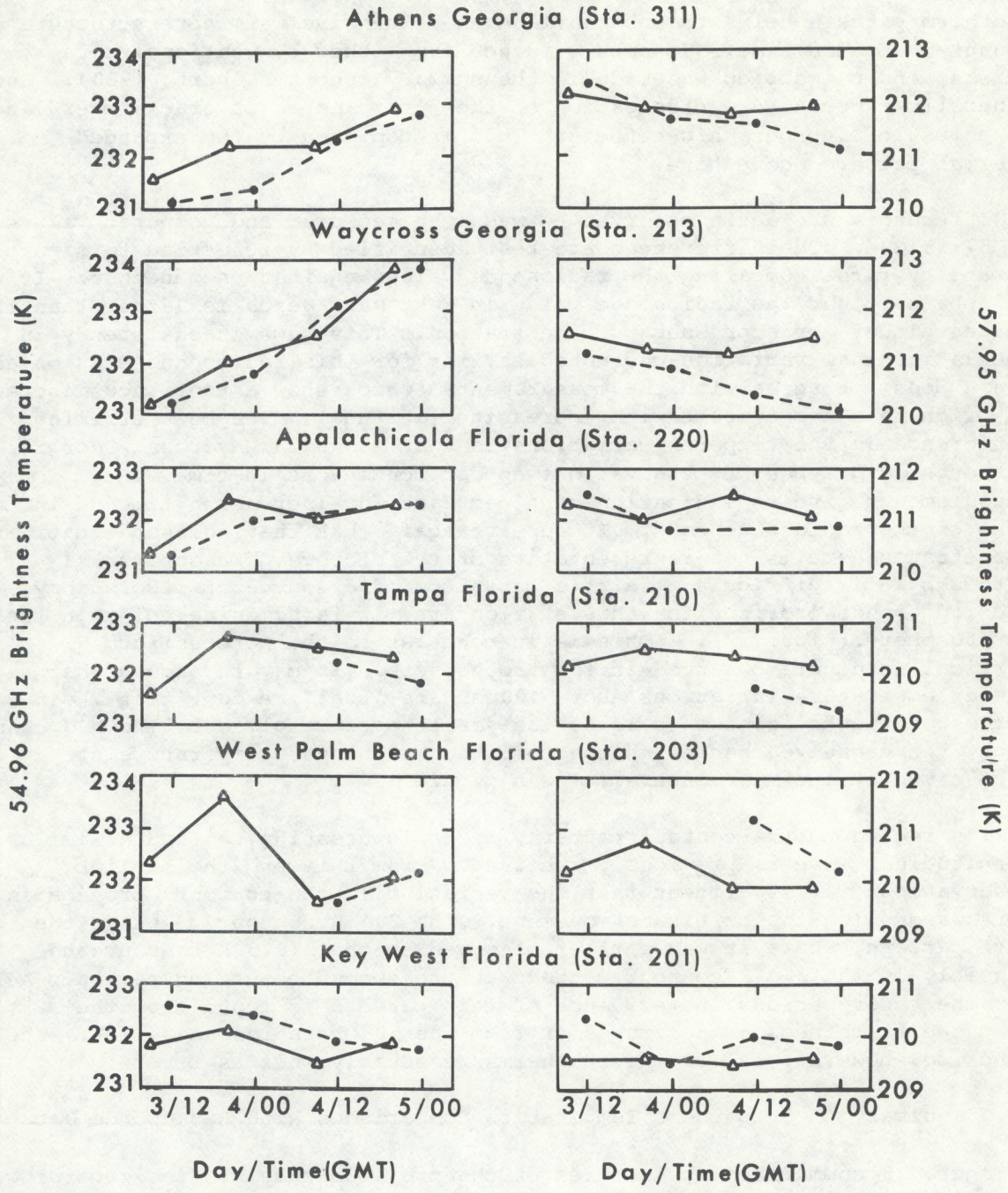

Figure 12. Time cross sections (Sept. 3-5, 1979) of brightness temperatures at 54.96 GHz (left) and 57.95 GHz (right) based on measurements (solid line) and radiosonde computations (dashed line). Measurements have been interpolated to radiosonde locations but are displayed at MSU observation times. Biases in measurements (figure 13) have been removed. These comparisons are for radiosondes along the hurricane track and indicate the largest differences for the 57.95-GHz channel.

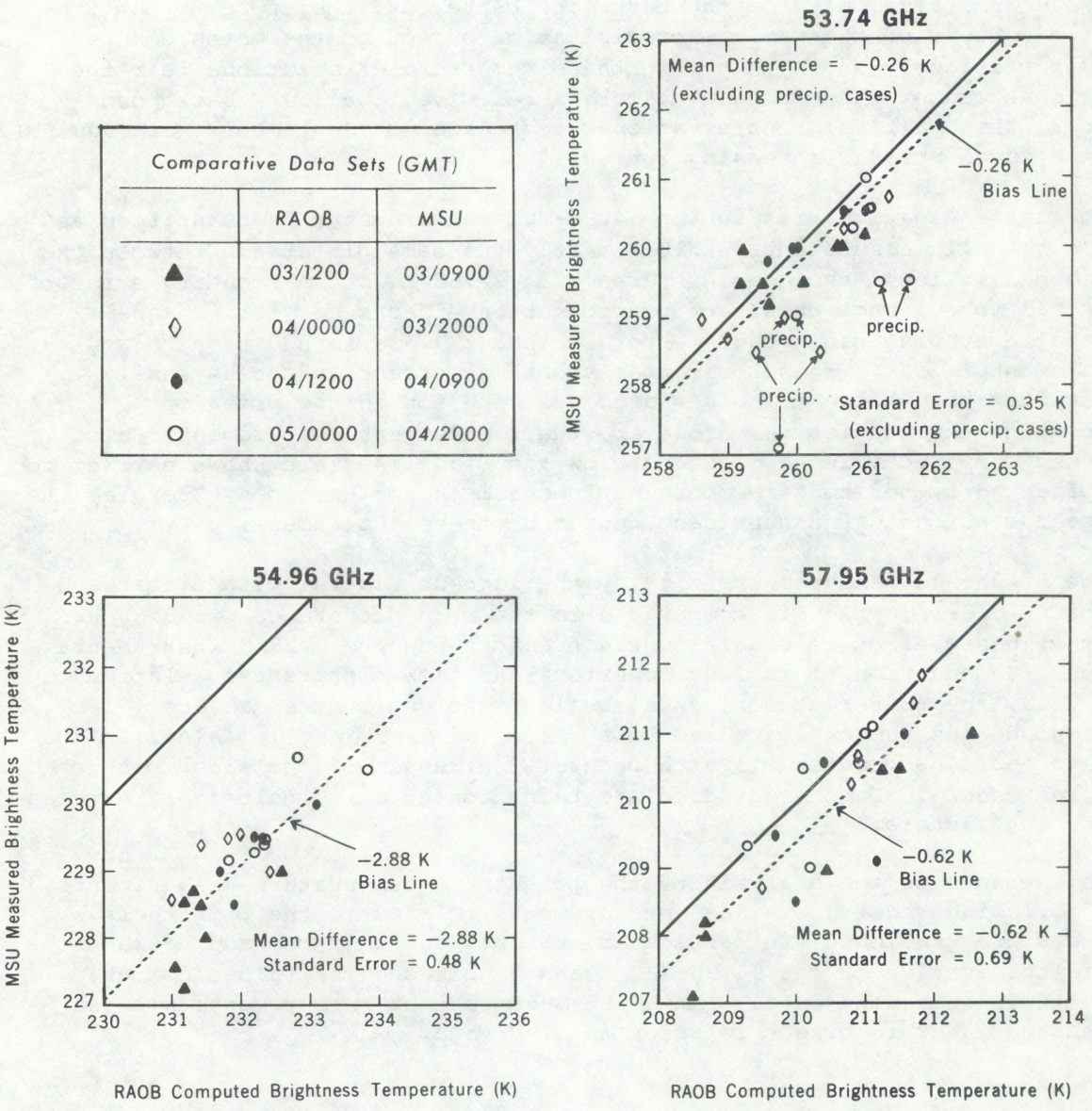

Figure 13. Summay of brightness temperature comparisons with radiosonde data for MSU channels (53.74, 54.96, 57.95 GHz). Solid line represents perfect correlation. Each scatter diagram contains the mean difference, standard error and bias line. The symbols used in the scatter diagrams are defined in the accompanying table. The largest standard error occurs for the 57.95-GHz channels with the smallest error at 53.74 GHz (excluding precip. cases).

The 53.74-GHz measurements influenced by precipitation (previously identified) are indicated on the scatter diagram but are excluded in obtaining the statistics. The "uncontaminated" data are shown to have a negligible mean difference (-0.26 K) and an equally small standard error (0.35 K) compared to the radiosonde values. Liquid water attenuation is seen to produce lower brightness temperatures by as much at 2.8 K. Unfortunately, the radiosondes located in precipitating regions are greater than 100 nmi (185 km) from the hurricane center and therefore do not provide a measure of the maximum precipitation effect on the measurements. It was previously shown that brightness temperature variations near the hurricane center can decrease up to 5 K relative to a 260 K background value. This particular observation was obtained on September 4 at 0900 GMT in the level-5 radar intensity region.

The large negative bias in the 54.96-GHz measurements is quantified as follows: All measurements exhibit nearly the same difference between the radiosonde values; the mean difference is -2.88 K with a standard error of 0.48 K. No evidence exists of precipitation effects for this channel. Spatial averaging can produce errors of about 0.5 K in addition to any instrumental bias. This horizontal smoothing effect is not as easily identified here because the measurements were not edited prior to generating the statistics. However, the two largest measurements (also largest computed values) plotted below the bias line were shown earlier to be affected by horizontal smoothing (comparison for Waycross, Georgia, the closest station to the hurricane center at these two times).

The 57.95-GHz measurements display the largest scatter with a standard error of 0.69 K, which is comparable to the mean difference of -0.62 K. This standard error is significantly greater than the 0.25 K instrumental noise. In addition to radiosonde errors and time differences relative to MSU data, the different horizontal scales resolved by the MSU and radiosonde instruments can lead to a source of discrepancy. Also, in the stratosphere, a greater mismatch occurs as a result of the slant path of the radiosonde. Further studies are being conducted to help isolate these different factors.

This concludes the analysis of the brightness temperature measurements. The following section examines measurements related to the brightness temperature gradient. In particular, comparisons will be made between the radial derivative of the 54.96-GHz measurements and the values computed from radiosonde wind data. The 57.95-GHz gradient measurements will be discussed later in direct relation to wind data.

4. BRIGHTNESS TEMPERATURE DERIVATIVE

4.1 General Considerations

Based on the thermal wind relationship, the radial derivative of brightness temperature, $\partial T_B/\partial r$, is directly related to the vertical weighted tangential wind (Grody et al., 1979);

$$R \frac{\partial T_B}{\partial r} = \int_{\ln p_s}^{\infty} \left(\frac{v^2}{r} + fv \right) \frac{d^2 \tau(p)}{d \ln p^2} \, d \ln p \qquad (2)$$

where v is the tangential velocity (positive for cyclonic flow), r is the distance from the hurricane center, f is the Coriolis parameter, and R is the gas constant. To simplify the notation, the frequency dependence associated with the transmittance and brightness temperature is not explicitly shown. Also, the equation contains no surface term since it is written mainly for the 54.96-GHz channel which has a negligible surface wind contribution.

Observe from eq. (2) that the radial acceleration term in the integrand is weighted by the vertical derivative of the temperature weighting function. The kernel $-d^2 \tau(p)/d \ln p^2$ is called the wind weighting function since it operates analogous to the temperature weighting function in eq. (1). However, unlike eq. (1), eq. (2) is model dependent. The thermal wind relationship used in deriving the equation assumes steady-state conditions. This is approximately true for well developed meteorological systems and has been used for hurricanes. To be more accurate in using eq. (2), the radial distance contained in the centrifugal acceleration component should be replaced by the radius of trajectory curvature. Also, the tangential winds should exclude the component arising from the hurricane's translational motion. For this reason, only tangential winds relative to the storm's movement are used when applying eq. (2). Although no provisions are made to include the effects of noncircular motion of the air parcel above 100 mb where the winds are less influenced by the hurricane, the centrifugal acceleration term is neglected compared to the Coriolis term.

To illustrate the tangential wind structure associated with hurricanes and the corresponding brightness temperature derivatives at 54.96 GHz, a simulation is performed using a representative sample of radiosonde wind (RAWIN) data for Hurricane David. For comparison, the same radiosonde station (Sta. 213 in Waycross, Georgia) is used that provided the thermal data displayed in figure 7. Figure 14 (right) displays the "relative" tangential winds obtained from the radiosonde data at three consecutive observation times beginning on September 4 at 0000 GMT and ending 24 h later when David was closest to the station. The relative winds are obtained by subtracting the 10 kn (5 m/sec) northerly directed hurricane motion. The table above the profiles gives the radiosonde time and distances of the three soundings from the hurricane. As with the temperature profiles in figure 7, these winds are characteristic of tropical cyclones, i.e., strongest winds towards the center (peaking near 850 mb), veering and becoming more anticyclonic with height (Frank, 1977).

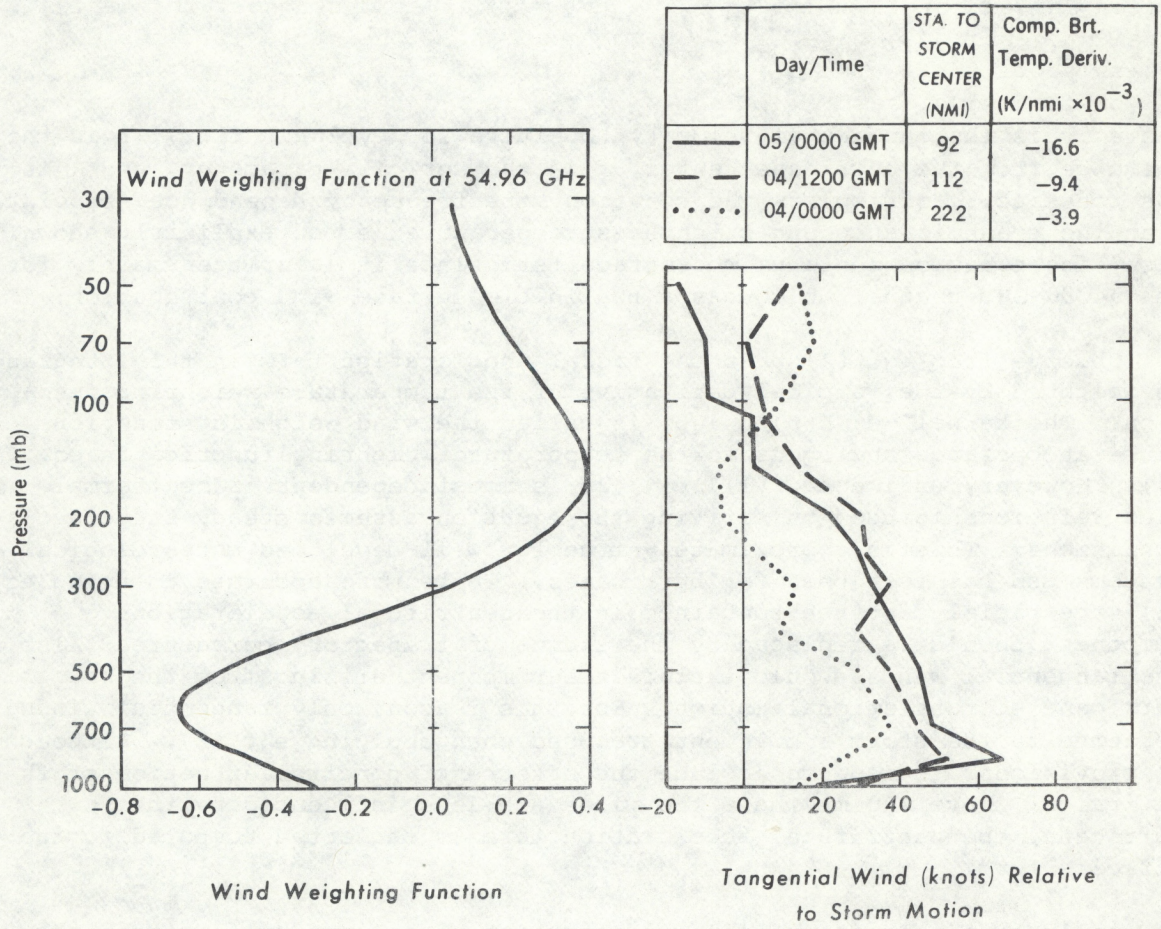

Figure 14. Radiosonde tangential wind profiles (right) at the same location (Sta. 213 in Waycross, Georgia) and time intervals as that of figure 7. Wind weighting function computed at nadir for the 54.96-GHz channel is shown for reference (left). Table indicates radiosonde times, distance from hurricane, and computed radial derivative of brightness temperature.

As indicated by eq. (2), the radial derivative of brightness temperature depends on the vertically integrated tangential wind according to the wind weighting function. Figure 14 (left) shows the wind weighting function at nadir for the 54.96-GHz channel which was computed from the derivative of the temperature weighting function in figure 2. The function is bimodal with the zero crossing at the peak level of the temperature weighting function and has equal areas above and below the crossover point. The derivative calculations are listed in the table of figure 14 for the different profiles. Note that the derivative is expressed in units of degrees Kelven per 1000 nmi (K/nmi x 10^{-3}) as it is throughout this study. It is interesting to observe the large changes in the derivative for what appears to be small differences in the wind profiles particularly in the case of the two closest soundings. This arises from the large changes in the centrifugal component of radial acceleration near the hurricane center. Compared to the brightness temperature changes shown in the table of figure 7, the radial derivative is much more variable near the hurricane center. As such, the effects of horizontal averaging and insufficient sampling are expected to be more pronounced in the derivative measurements.

4.2 Measurements

Figure 15 presents the hand-analyzed fields of the brightness temperature derivative at 54.96 GHz for the four observation times of this study. Finite-difference techniques are used to compute the radial derivative from the brightness temperature measurements. This is accomplished by first positioning the measurements on a cylindrical coordinate map centered about the hurricane center, which is approximated by the location of the maximum brightness temperature. The measurements are then interpolated to grid points with 50-km equal spacing along 24 radial lines, each line being separated by 15° of azimuth angle. A five-point smoothing procedure is introduced to reduce any noiselike variations in the brightness temperature field prior to obtaining the derivative. This smoothing procedure is found to only alter the derivative values far from the hurricane center, i.e., for regions beyond the third scan position from nadir. Note that most of the area shown in figure 15 is within four scan positions from nadir, where the dashed straight line on each map indicates the nadir track. Each map also contains the computed derivative values based on eq. (2), using the radiosonde wind data as previously described. To minimize errors in the computation, only those radiosondes reporting winds up to at least 50 mb were used. Above this level, the soundings were continued using time-interpolated radiosonde data whenever possible.

At the earliest time of September 3 at 0900 GMT, the derivative field has an asymmetric structure with larger derivatives extending farther into the northeast quadrant of the hurricane. This would indicate larger tangential winds in this area. The four computed values are seen to compare reasonably well with the contour analysis. Before continuing with the next period, it is instructive to compare this derivative map with the brightness temperature map in figure 8. Observe that the large derivatives in the southeast corner correspond to the tighter brightness temperature contours in this region. Also, the smallest derivatives around the northwest corner are associated with the relatively uniform brightness temperature field there.

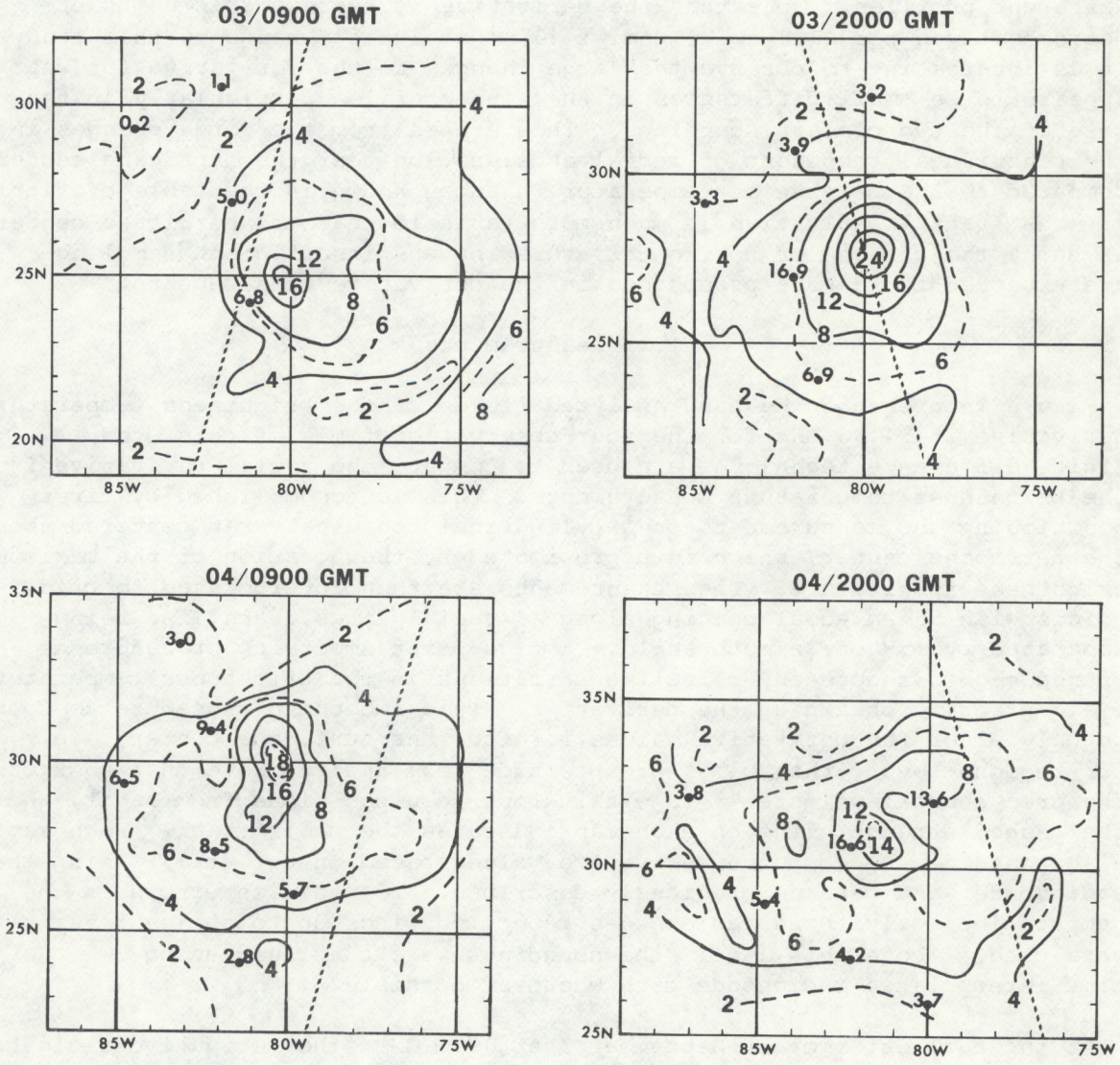

Figure 15. Radial derivative of 54.96-GHz brightness temperature measurements at indicated observation times. Each contour map also contains the computed derivatives (K/nmi x 10^{-3}) based on the radiosonde winds. (See text.) The straight dashed line represents the nadir track. The largest differences between measured and computed values occur near the hurricane center (indicated by highest contour value).

The results 11 h later are quite different. Compared with the previous time, the maximum contour value has increased from 16 to 24 derivative units. Also, the pattern is more symmetric than before. This larger central derivative would indicate an increase in intensity, assuming no substantial increase in size around the eye region. As observed in the case of Typhoon June (Rosenkranz et al., 1978), changes in the eye dimensions affect the spatially averaged brightness temperature measurements and must be considered when comparing the magnitude of the temperature anomaly at different times. This can lead to misinterpretations of the measurements around the hurricane center, particularly with regard to the derivative measurements (Grody et al., 1979). The influence of horizontal resolution is observed from the comparisons between the measured and computed derivatives. Note that the four computed values located farther from the hurricane center compare better with the contours than the closest computed value of 16.9 units shown on the 6-unit contour.

Continuing with the data obtained on September 4 at 0900 GMT, the central value has decreased to 18 units, suggesting a reduction in hurricane intensity. Also, the pattern appears less symmetric than the previous case, indicating the possibility of stronger winds in the southwest quadrant where the larger derivative exists. Comparisons with computed values again reveal the effects of horizontal resolution on the measurements. Of the six computed values, the two closest values of 8.5 and 9.4 units are significantly larger than the surrounding contour values.

The last period of September 4 at 2000 GMT shows the least structure for the derivative field. The maximum contour value has dropped to 14 units, the smallest value of the four periods. Also observed is a rather diffuse pattern, consistent with the expanded brightness temperature field shown in figure 11. Compared with the computed values, one again finds the largest differences with the two closest radiosonde values, while the four radiosonde values farthest from the center compare better with the contour analysis.

A summary of the comparisons between measured and computed radial derivative of brightness temperature is shown in figure 16. The measured derivatives are plotted against the computed values for the four time periods. As in the case of the brightness temperature comparisons, the different data sets are indicated by different symbols. Also, to aid in the interpretation of the results, the radial distance to the hurricane center is indicated next to each symbol. Note that the largest differences between measured and computed values occur for the matchups close to the hurricane center. In general, the results are reasonably good for distances greater than about 150 nmi (275 km), where these data do not depart markedly from the straight line which indicates perfect correlation.

5. TEMPERATURE AND WIND DETERMINATIONS

This last part of the study examines the application of the sounding channels for deriving temperatures and winds at specific levels in the atmosphere. The so called retrieval problem involves the inversion of eqs. (1) and (2) to estimate the meteorological parameters contained in the integrand from the integral related measurements. Algorithms will be developed and compared with data obtained from Hurricane David.

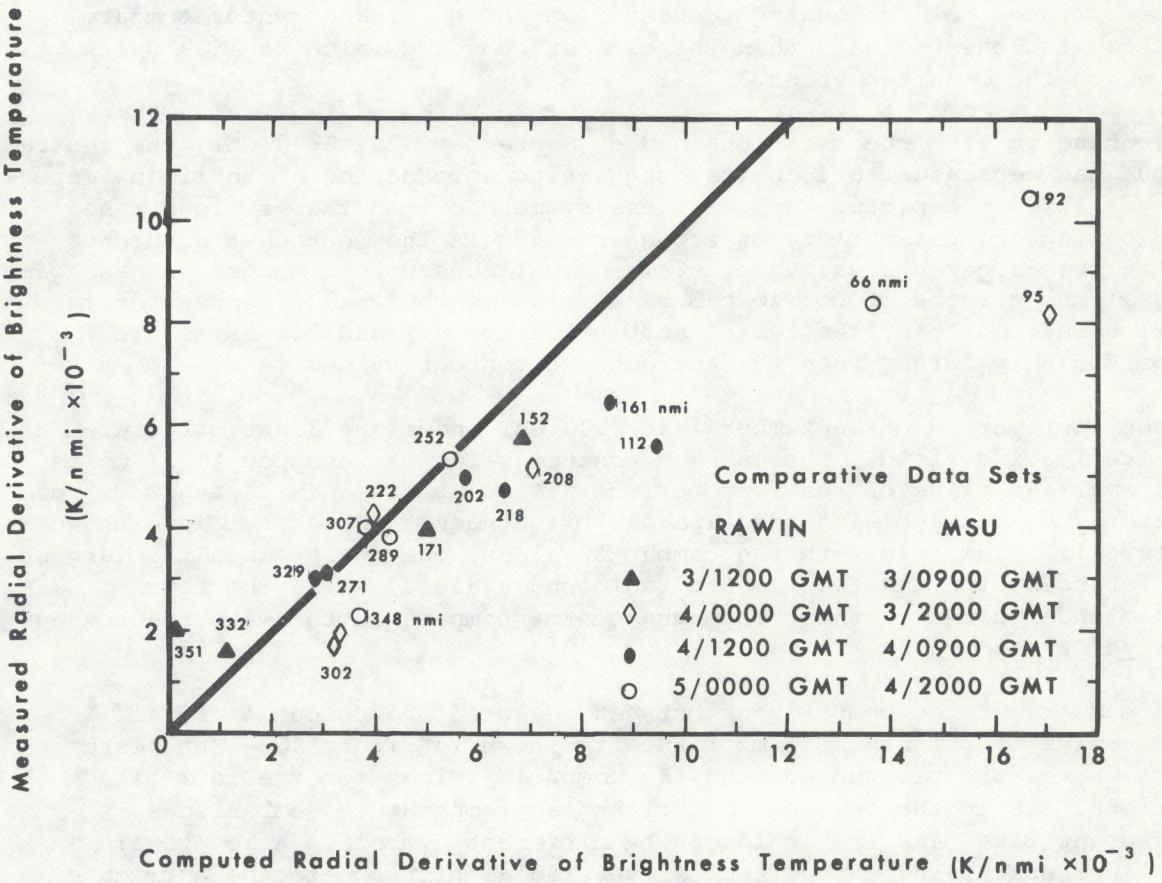

Figure 16. Comparisons between measured and computed radial derivative of 54.96-GHz brightness temperature. Solid line represents perfect correlation. Distances (nmi) between data and hurricane center are inserted next to data symbols. (See table.) The largest differences between measured and computed values occur close to the hurricane; measurements underestimate the brightness temperature derivative.

5.1 Temperature Determination

Based on the relationship between brightness temperature and temperature given by eq. (1), temperature profiles have been derived (retrieved) by linearly combining the different sounding channel measurements to invert the radiative transfer equation. The success of the inversion procedure to reconstruct the temperature profile depends on the number of sounding channels and the vertical structure of the "actual" temperature, in addition to other factors (Grody, 1980). In the midlatitudes where temperature variations are large and liquid water effects are generally small, the temperature retrievals can provide additional information to complement the available radiosonde data. However, as already shown, the precipitation effects during tropical storms can dominate the response of the lower MSU sounding channel (53.74 GHz), and the temperature variability is relatively small. This presents a number of problems in obtaining accurate temperature retrievals for the purpose of improving the conventional analysis in the tropics.

Linear regression techniques have been used successfully for providing temperature retrieval algorithms (e.g., Waters et al., 1975; Grody and Pellegrino, 1977) and will be applied here. The temperature at any pressure level is expressed as a linear combination of the brightness temperatures, viz.,

$$T(p) = a_o(p) + \sum_{n=1}^{N} a_n(p)\, T_B(\nu_n) \qquad (3)$$

where the regression coefficients a_n depend on the correlation between the temperature at a particular level and the brightness temperatures of the "N" sounding channels. Only the 54.96- and 57.95-GHz channels are considered in regard to tropical storms, although it would be possible to utilize the 53.74-GHz channel outside the precipitation regions. As in the above referenced studies, the regression coefficients are determined using a representative set of radiosonde data and the corresponding computed brightness temperatures. Two different sets of radiosonde data will be considered, a climatological set of 400 tropical soundings and those soundings collected for the Hurricane David case. Comparisons will be made between the results in the two cases.

In the case of the climatological data set, 400 tropical soundings were acquired over the globe for all seasons. To synthesize the limb-corrected and emissivity-normalized brightness temperatures, the radiative transfer equation (1) was applied considering a unity emissivity surface viewed at nadir. Liquid water effects were included by inserting layers of liquid water (density between 0 to 1 g/m^3) in a random manner between the surface and 300 mb level throughout the 400 soundings. Regression coefficients are generated by correlating the brightness temperatures (containing an additive 0.3K rms noise) with the radiosonde temperatures. Both one- and two-channel algorithms were obtained and, when applied to the dependent data set, resulted in the error characteristics shown in figure 17. It should be mentioned that the retrieval errors are found to be essentially the same when clouds are eliminated in the brightness temperature simulations.

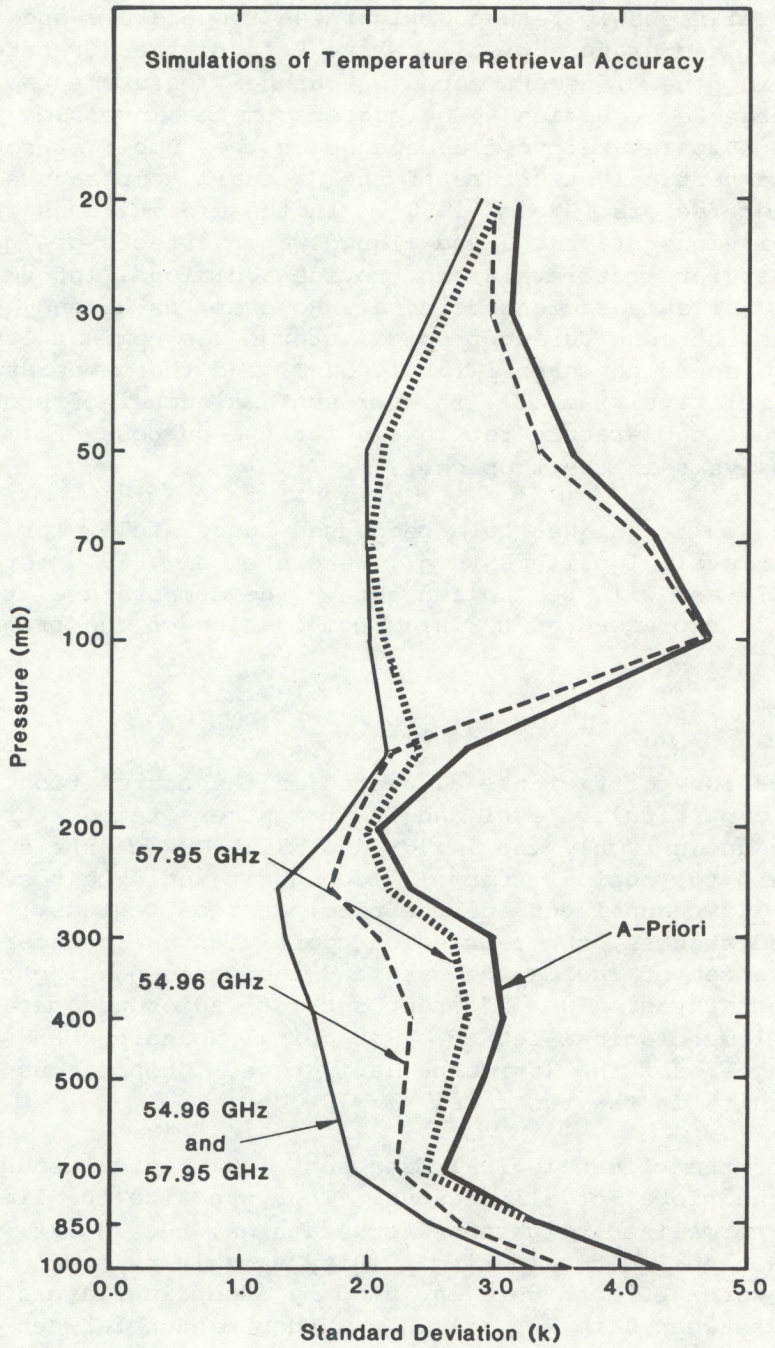

Figure 17. Simulated accuracy of temperature retrievals based on 400 global, all season, tropical radiosonde profiles. Standard errors are shown for the 54.96- and 57.95-GHz channels used separately (dashed lines) and in the combined mode (solid line). The heavy solid line (a-priori) shows the standard deviation of the radiosonde temperatures.

The standard errors shown in figure 17 are based on the 54.96- and 57.95-GHz channels used separately as predictors and in the combined mode. Also shown is the standard deviation (a-priori) of the 400 tropical soundings, which serves as a guide in determining the information content of the different channel combinations. As expected, the 54.96-GHz channel is the best single predictor in the troposphere, while the 57.95-GHz channel is dominant in the stratosphere. Since the separation between the standard error and a-priori is a measure of the information content, it is apparent that the 54.96-GHz channel provides most information within the 250- to 500-mb layer, while the 57.95-GHz channel is extremely useful for estimating temperatures between 150- and 30-mb. The region of maximum information is partly defined by the location and shape of the weighting functions (figure 2) and partly by the statistical correlation between the weighted temperature (brightness temperature) and the temperature at a particular level.

As an example of strong statistical correlation, note (figure 17) the large error reduction in the troposphere due to the addition of the 57.95-GHz channel in the two-channel algorithm. No such large effect is observed in the stratosphere when the 54.96-GHz channel is added in the two-channel algorithm. For comparison purposes, the one- and two-channel algorithms are given for the 300 mb level:

$$T(300) = - 146.71 + 1.67\ T_B(54) \qquad (4a)$$

$$T(300) = - 80.44 + 1.92\ (T_B(54) - 0.30\ T_B(57)) \qquad (4b)$$

where the temperature and brightness temperatures are in K.

The two-channel algorithm contains a negative relationship between the 57.95-GHz brightness temperature $T_B(57)$ and the temperature at 300 mb. Such negative correlation is found throughout the troposphere up to 200 mb and is responsible for the large error reduction shown in figure 17. It is interesting to compare these climatological results, which represent the majority of tropical atmospheres, with the more specific hurricane situation. Data obtained for Hurricane David are applied to obtain the regression algorithms and the statistical results.

In section 3, a total of 23 radiosonde profiles were used to compute brightness temperatures for the 54.96- and 57.95-GHz channels (figure 13). These soundings extended up to at least 30 mb and are between 100 nmi (185 km) and 500 nmi (925 km) of the hurricane center. We now examine the retrieval algorithms generated by these data. As before, the regression coefficients are obtained by correlating the computed brightness temperatures with radiosonde data. Liquid water effects are excluded since it was previously found that the influence of clouds produces no significant change in the algorithms or error characteristics. The resulting statistics are shown in figure 18(a), using the same parameters as in the climatological

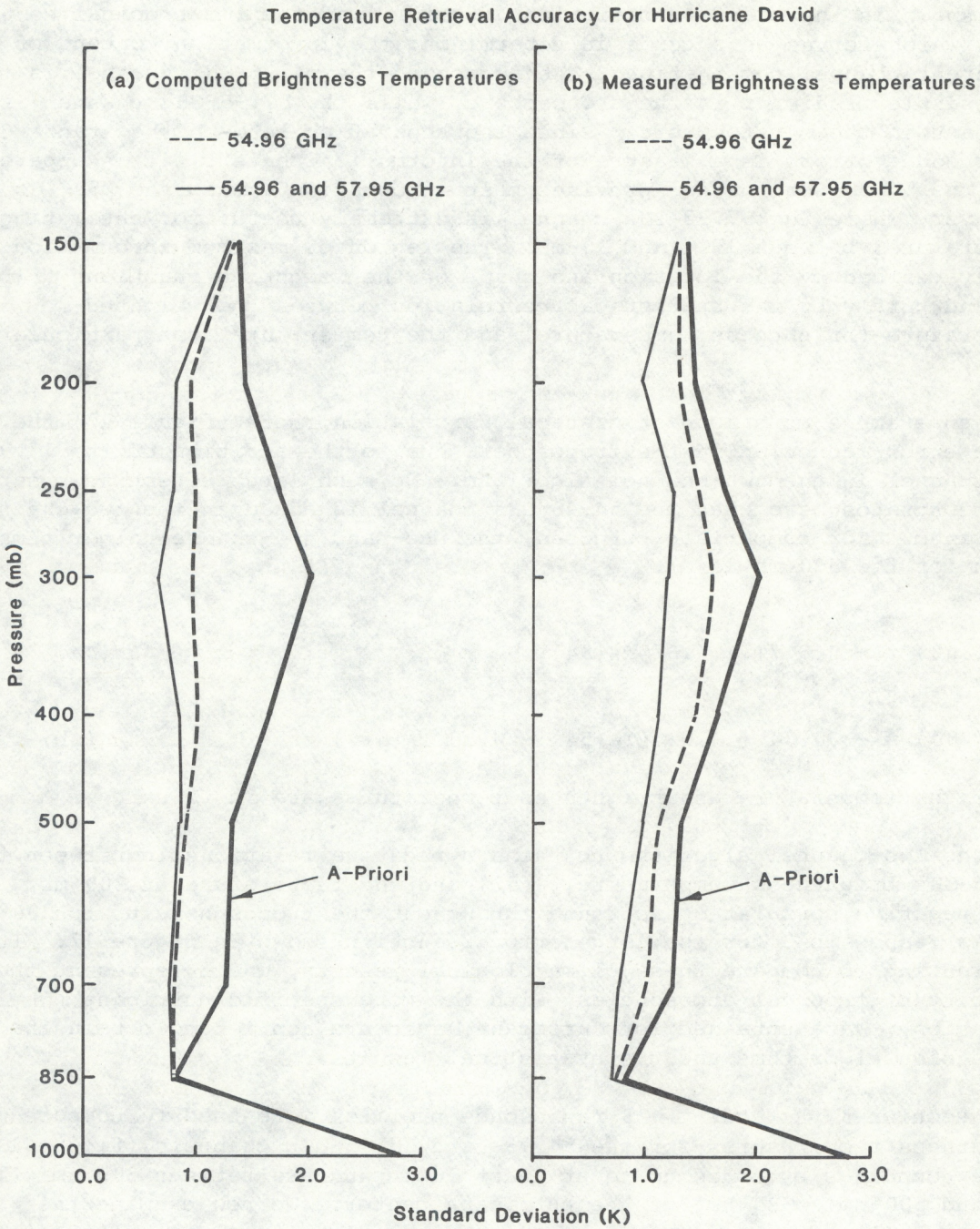

Figure 18. Temperature retrieval accuracy for Hurricane David. Retrieval errors are shown based on (a) computed and (b) measured brightness temperatures. Both one-channel (54.96 GHz) and two-channel (54.96 and 57.95 GHz) standard errors are plotted along with the standard deviation (a-priori) of the radiosonde sample.

study. Unlike the results of figure 17, there is no significant improvement when the 57.95-GHz channel is added in the two-channel solution. The algorithms for the 300 mb temperature are now given by

$$T(300) = - 331.93 + 2.48\ T_B(54) \tag{5a}$$

$$T(300) = - 180.75 + 2.42\ (T_B(54) - 0.27\ T_B(57)) \tag{5b}$$

and differ from the climatological results of eq. (4a) and eq. (4b). Of particular significance is the larger weight placed on the 54.96-GHz channel in both algorithms for the case of the hurricane. However, relative to the 54.96-GHz coefficients, the negative weight applied to the 57.95-GHz channel is about the same in eq. (4b) and eq. (5b). The little improvement seen in figure 18(a) when applying the 57.95-GHz channel, is obviously not solely due to the different weight of this channel compared to the climatological case. What is suggested is that the 57.95-GHz channel is less correlated with the tropospheric temperature (and with the 54.96-GHz channel) than in the case of the more general tropical atmospheres. Unfortunately, however, the 57.95-GHz computed brightness temperatures in section 3 were found to be inconsistent with the measurements. Therefore, as a final comparison with the climatological results, we consider the retrievals based on the measured brightness temperatures.

In addition to obtaining coefficients using computed brightness temperatures, the regression procedure is applied to the measurements obtained for Hurricane David. The brightness temperature measurements are those plotted in figure 13 and correspond to the same 23 radiosonde profiles used above. Figure 18(b) shows the standard errors based on the measurements. These errors are larger than those in the adjacent diagram which are based on computed brightness temperatures. In the case of the one-channel algorithm, the larger errors arise from factors such as instrumental noise and horizontal smoothing associated with the measurements. As shown in figure 13, these effects produce a standard error of 0.48K when compared against the computed brightness temperatures. Although the two-channel results are also more erroneous in the case of the measurements, the 57.95-GHz channel provides a larger relative improvement compared to the computed brightness temperature results given in figure 18(a). This is more consistent with the climatological case and results from the 57.95-GHz measurements being more representative than the computed values. Recall that the large standard error of 0.69K between the measured and computed brightness temperatures (fig. 13) was attributed to inconsistency of the radiosonde data in the stratosphere, among other factors.

The physical reason for the improvement using the 57.95-GHz measurements is illustrated by the sample measurements in figure 5. Observe that the 54.96-GHz channel displays a slight latitudinal increase in brightness temperature due to the stratospheric contribution (evident from the weighting function in figure 2). The 57.95-GHz channel responds to this portion of the atmosphere, as evidenced by the strong latitudinal variation observed in the measurements, and therefore compensates for the latitudinal changes noted in

the 54.96-GHz channel. Throughout this study, no such consistent latitudinal variation was apparent in the computed brightness temperatures at 57.95-GHz. However, in addition to any statistical correlation between the stratospheric and tropospheric temperatures, this compensation offered by the 57.95-GHz provides the improvements seen in the two-channel algorithm of figure 18(b).

As before, the 300 mb temperature algorithms are now presented based on the measured brightness temperatures:

$$T(300) = - 78.69 + 1.40\ T_B(54) \tag{6a}$$

$$T(300) = - 71.13 + 2.38\ (T_B(54) - 0.46\ T_B(57)) \tag{6b}$$

Compared to that of eq. (5a), the 54.96-GHz channel is given less weight by the single-channel algorithm because of the smoothing and noise introduced by the brightness temperature measurements compared to the computed values. However, the measurements for the 57.95-GHz channel are considered more representative than the computed values and result in a larger negative coefficient in eq. (6b) than that of eq. (5b). This stronger correlation between the 300 mb temperature and upper sounding channel is reflected in figure 18(b) and results in a greater relative improvement in retrieval accuracy compared to the adjacent diagram.

5.2 Wind Determination

The similarity between eq. (1) and eq. (2) suggests an analogy between the temperature and wind retrieval methods. Following the arguments leading to the temperature retrieval algorithm of eq. (3), we write

$$\frac{V^2(p)}{r} + f\ V(p) = b_o(p) + \sum_{n=1}^{N} b_n(p)\ \frac{\partial T_B(\nu_n, r)}{\partial r} \tag{7}$$

where the regression coefficients b_n now depend on the correlation between the winds (more explicitly the radial acceleration at a particular pressure level) and the brightness temperature radial derivative of the "N" sounding channels. Unlike the derivation of the temperature retrieval coefficients, where a climatological data base was available, no such data set exists for winds. As such, these coefficients are generally determined in an indirect manner by incorporating the temperature retrieval coefficients and therefore eliminating any statistical correlation between winds and the derivative measurements (Grody, 1978). The unique wind characteristics in the case of hurricanes require that more special attention be paid to the statistical correlation. For this reason, only the results derived from the Hurricane David data will be presented. As already mentioned, only the 54.96-GHz channel responds to the tropospheric circulation pattern of the hurricane, so that this channel alone will be considered in determining tropospheric winds.

The 21 radiosonde wind observations displayed in figures 8 through 11 were used to compute the radial derivative of brightness temperature at 54.96 GHz using eq.(2). These computed values were shown in figure 16 along with the measured values. The regression coefficients in eq. (7) are obtained by correlating the 21 derivative values with the corresponding radial acceleration at specific pressure levels. Applying the algorithms to the dependent data results in the derived quantities shown in figure 19. These are plotted against the radial derivatives at the indicated pressure levels. The regression equations at the different pressure levels are given by the straight lines shown on each diagram and result in the correlation coefficients indicated. According to the scatter diagrams, the best correlation occurs around the 700 to 500 mb region, i.e., within the lower mode of the wind weighting function. This high correlation in the lower troposphere supports the close correspondence observed earlier between the measurements and the 700 mb wind directions. However, upon applying these algorithms to the actual measurements, the reduction in amplitude of the measured radial derivative (figure 16) would produce underestimates of the tangential wind near the hurricane center. Although empirical adjustments can be made (Grody et al., 1979), the fact remains that greater horizontal resolution with proper sampling is needed to resolve the large brightness temperature derivatives associated with hurricanes.

It is interesting to compare the wind with the temperature retrievals based on the computed brightness temperatures at 54.96 GHz. The temperature retrieval algorithms were described earlier and applied to the 23 radiosonde profiles to generate the statistical results in figure 18(a). We now examine the error characteristics at specific pressure levels by plotting the temperature retrievals against the computed brightness temperature (figure 20). The straight lines define the one-channel retrieval algorithms at the different pressure levels, where the correlation coefficient is indicated on each diagram. Compared with the wind retrievals (figure 19), the maximum correlation is much less for the temperatures. Also, temperature is best derived at 300 mb near where the temperature weighting function peaks, while the wind retrieval is optimized around the lower mode peak of the wind weighting function. The higher correlation associated with winds is due to the more restricted variability of radial acceleration compared to temperature. That is, much of the variation in the radial acceleration is found below the 300 mb crossover point of the wind weighting function, while the temperature variations occur throughout much of the temperature weighting function. In essence, only about half the area of the temperature weighting function contributes to wind retrieval, compared to the larger area contributing to temperature retrieval.

For stratospheric wind retrieval, only the 57.95-GHz channel is considered. Although not shown, the wind weighting function is similar in general appearance to that of the 54.96-GHz channel (figure 14) except for the vertical displacement of the crossover point to about 90 mb. However, unlike the 54.96-GHz channel whose gradient field is mainly in the radial

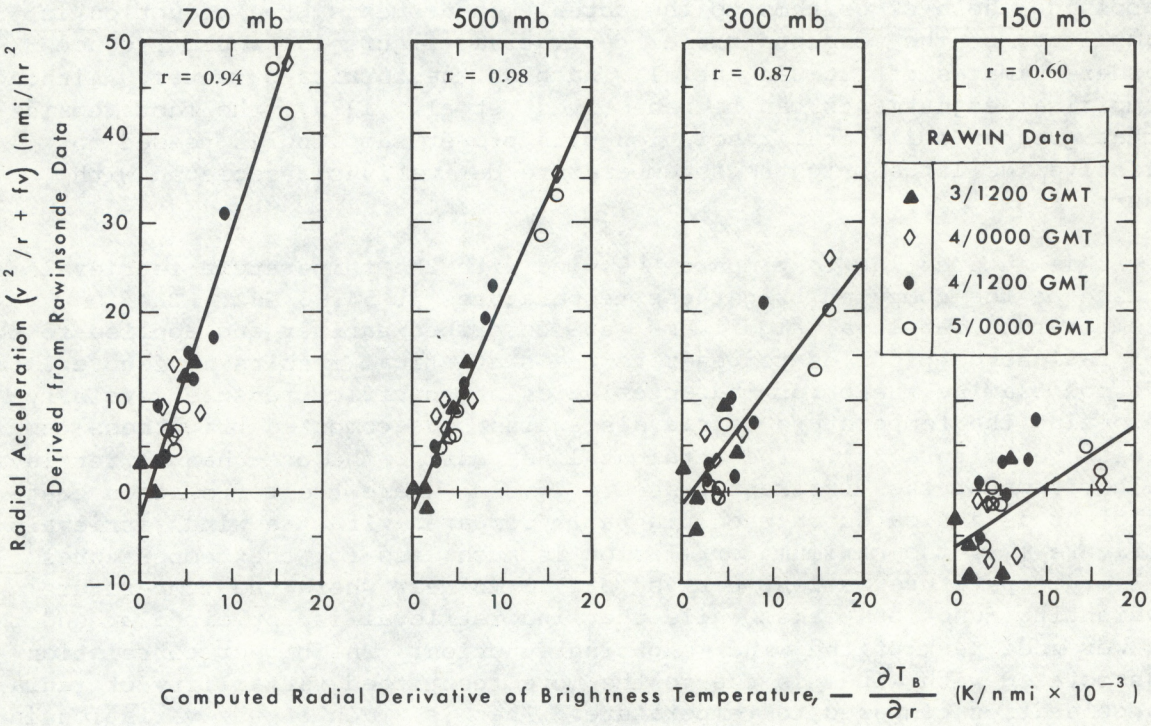

Figure 19. Winds (radial acceleration at indicated pressure levels) compared against computed 54.96-GHz brightness temperature radial derivative. The regression equations at the different pressure levels are represented by straight lines with the correlation coefficients shown at top of each scatter diagram. Table (right) contains definition of symbols used in scatter diagrams. Highest correlation occurs for winds between 700 and 500 mb, corresponding to the lower mode of the wind weighting function (figure 14).

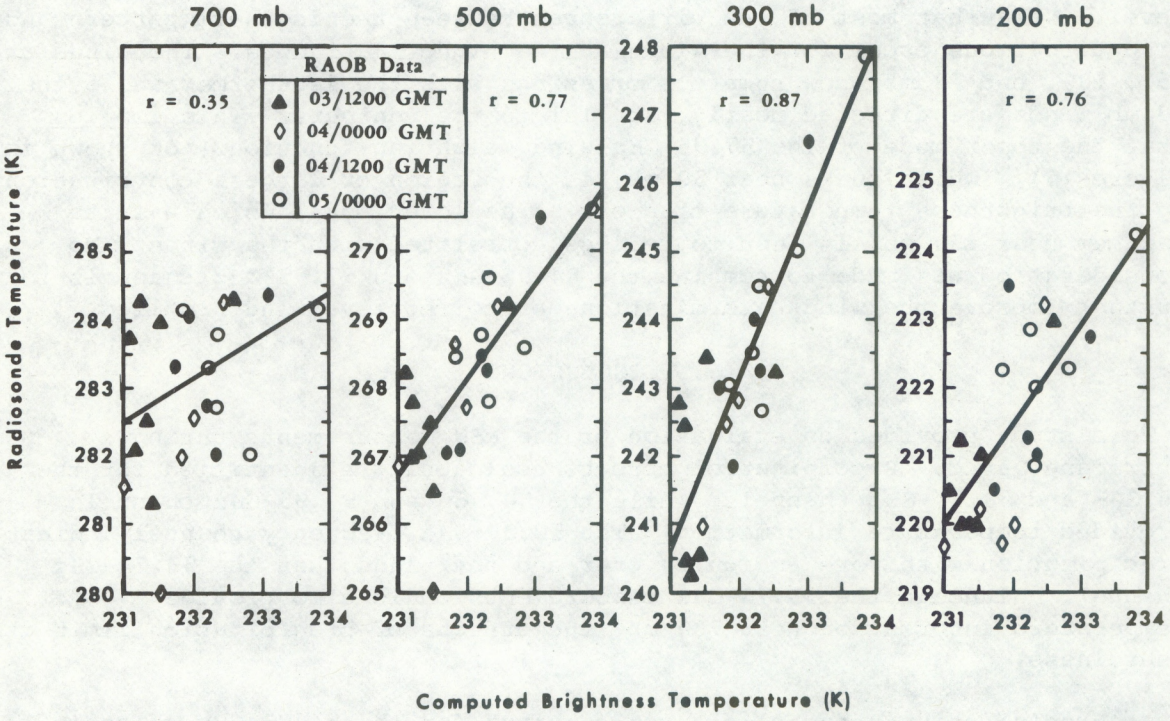

Figure 20. Radiosonde temperatures at indicated pressure levels compared against computed 54.96-GHz brightness temperature. The one-channel retrieval algorithms at the different pressure levels are represented by straight lines with the correlation coefficients shown at top of each scatter diagram. Highest correlation occurs for temperature near 300 mb, corresponding to the peak of the temperature weighting function (figure 7).

direction, the 57.95-GHz pattern is predominately oriented along constant latitude lines. This directional characteristic alone is sufficient for identifying the pressure level giving the best wind correlation. Radiosonde winds were plotted on separate maps at four levels, two above and two below the crossover point of the weighting function, and were compared with the 57.95-GHz brightness temperature measurements.

An example of the comparison procedure used above is shown in figure 21. The sample of the radiosonde wind data shown here is for September 4 at 0900 GMT, with respect to the MSU observations, and is a slightly smoother version of the brightness temperature field shown in figure 10. All four maps display the same brightness temperature field, but the radiosonde winds are shown at different pressure levels (150, 100, 70, and 50 mb). From such comparisons, it was concluded that the correspondence between the isotherm pattern and wind direction is best near the 50 mb level. Note that most of the differences between the isotherm pattern and wind directions occur for the winds at the higher latitudes. The winds at 150, 100, and 70 mb show numerous crossings with the isotherms, while the 50 mb winds are directed nearly parallel to the contours. This implies that the upper mode of the 57.95-GHz wind weighting function (not shown in figure 14), which peaks near 50 mb, is the region of largest contribution to the brightness temperature gradient. The lower mode, which has its maximum near 150 mb, is seen to be less correlated with the winds. No consideration was made to combine the 54.96-GHz and 57.95-GHz channels to further improve the wind determinations or to retrieve wind profiles.

6. CONCLUSIONS

This study provided an evaluation of the MSU measurements during Hurricane David. Precipitation effects could only be identified for the 50.30- and 53.74-GHz channels, while the 54.96- and 57.95-GHz channels provided temperature information. The 50.30-GHz frequency channel indicates precipitation with more ambiguity over and near land than the 53.74-GHz channel. Although the 53.74-GHz measurements could also provide temperature information near 700 mb, the effects of precipitation limit its usefulness.

Precipitation effects were not apparent for the 54.96-GHz channel. This channel responds to temperature near 300 mb and displays the warm-core structure of the hurricane. Also, the brightness temperature contours follow the 700 mb wind directions. This strong correlation between the low-level winds and the 54.96-GHz measurements is limited to directions only; higher spatial resolution is required to estimate wind speed.

The 57.95-GHz measurements correspond to temperature near 100 mb, so that the hurricane influence is minimal. The brightness temperatures reveal the large latitudinal change in tropopause height, while the pattern correlates best with winds around 50 mb. Compared with the radiosonde computed brightness temperatures, the 57.95-GHz measurements show the greatest disparity. This is attributed to a number of differences between the radiosonde and MSU measurements. In addition to radiosonde error and the horizontal resolution and time difference factors, there is a greater possibility of mismatch in the stratosphere because of the slant path of the radiosonde. Further studies are needed to isolate the major source of disparity observed in the stratosphere, although it does not appear to be associated with errors in the MSU measurements.

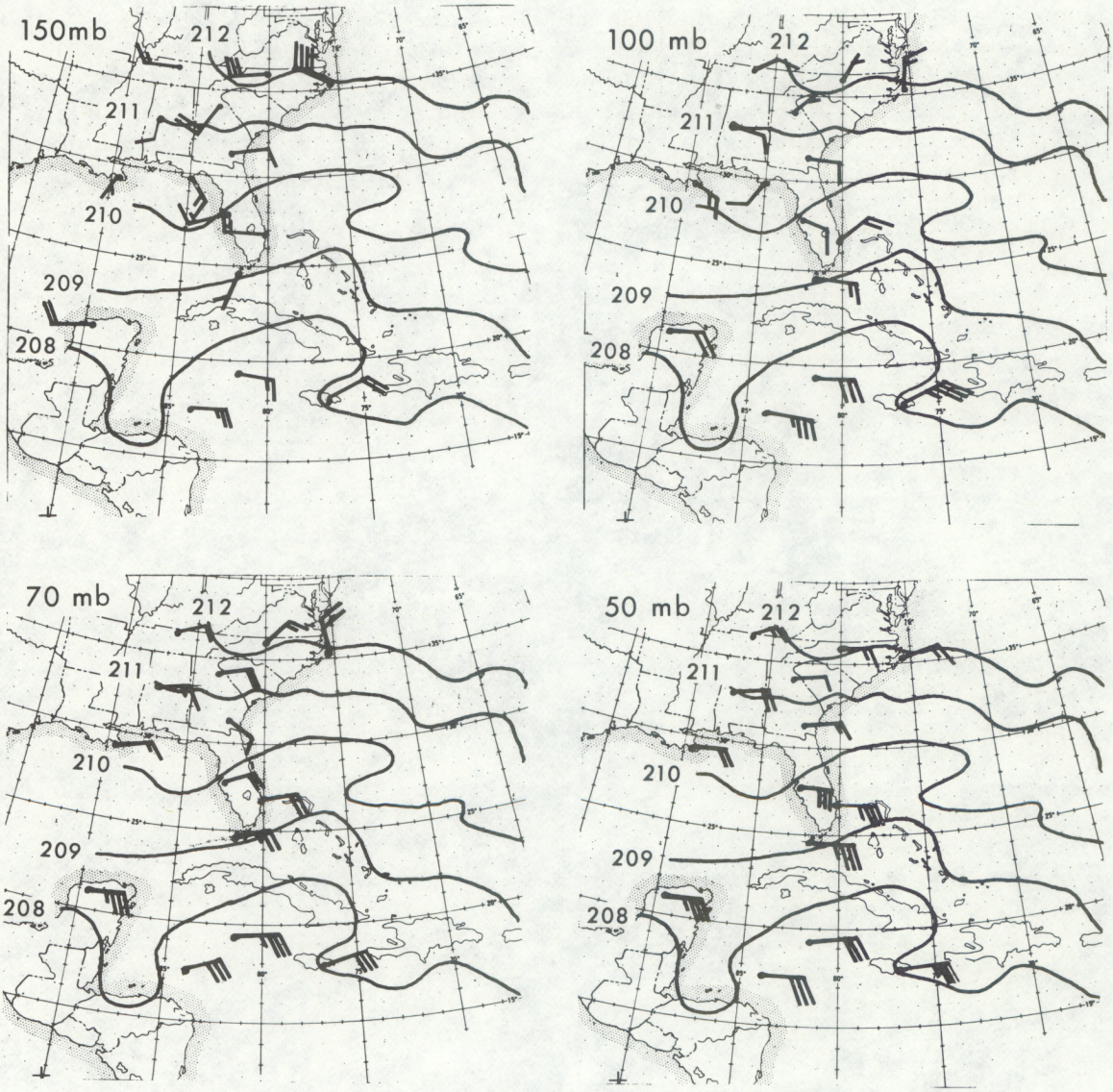

Figure 21. Comparisons between 57.95-GHz brightness temperature pattern (shown for September 4, 0900 GMT) and radiosonde winds at indicated pressure levels. From similar comparisons at other periods, it is determined that the contours best follow the directions of the 50 mb winds. Note that the brightness temperature field is a slightly smoother version of that shown in figure 10.

7. ACKNOWLEDGMENTS

We wish to thank and acknowledge the assistance of Mitchell Goldberg for providing programming support and Kay Collins for typing the manuscript. We are indebted to A. Timchalk and J. Lienesch for their helpful reviews of this report. Our appreciation goes to P. McHugh who painstakingly reviewed the report and provided numerous changes to enhance the meaning of the text.

8. REFERENCES

Allison, L.J., E.B. Rodgers, T.T. Wilheit, and R.W. Fett, 1974: Tropical cyclone rainfall as measured by the Nimbus 5 electrically scanning microwave radiometer. Bull. Amer. Meteor. Soc., 55, 1074-1089.

Dvorak, V.F., 1975: Tropical cyclone intensity analysis and forecasting from satellite imagery. Mon. Wea. Rev., 103, 420-430.

Feigelson, E.M., 1966: Light and Heat Radiation in Stratus Clouds. Israel Program for Scientific Translations Ltd., IPST Cat. No. 1528, 245 pp. (See p. 8.) Available from U.S. Dept. Commerce, Clearinghouse for scientific and technical information, Springfield, VA 22151.

Frank, W.M., 1977: The structure and energetics of the tropical cyclone--I. Storm structure. Mon. Wea. Rev., 105, 119-1135.

Fritz, S., L.F. Hubert and A. Timchalk, 1966: Some inferences from satellite pictures of tropical distrubances. Mon. Wea. Rev., 94, 231-236.

Grody, N.C., 1976: Remote sensing of atmospheric water content from satellites using microwave radiometry. IEEE Trans. Ant. Prop., 24, 155-162.

Grody, N.C. and P.P. Pellegrino, 1977: Synoptic scale studies using the Nimbus 6 scanning microwave spectrometer. J. Appl. Meteor., 16, 816-826.

Grody, N.C., 1978: Microwave radiometry applied to synoptic meteorology and climatology. In Applications Review Pannel Report, High Resolution Passive Microwave Satellites, edited by D.H. Staelin and D.W. Rosenkranz, Research Lab. Electronics, MIT, 8 chapters (see ch. 6).

Grody, N.C., C.M. Hayden, W.C. Shen, P.W. Rosenkranz, and D.H. Staelin, 1979: Typhoon June winds estimated from scanning microwave spectrometer measurements at 55.45 GHz. J. Geophys. Res., 84, 3684-3695.

Grody, N.C.., 1980: Analysis of satellite-based microwave retrievals of temperature and thermal winds: Effects of channel selection and a-priori mean on retrieval accuracy. In Remote Sensing of the Atmosphere and Oceans, Edited by Adarsh Deepak, Academic Press, 650 pp.

Hebert, P.J., 1980: Atlantic hurricane season of 1979. Mon. Wea. Rev., 108, 973-990.

Hubert, L.F., N.C. Grody, A. Timchalk, and W.C. Shen, 1981: The effect of precipitation on microwave soundings in low latitudes. NOAA Tech. Rept., NESS 82, pp. 34.

Ishimaru, A. and R.L.T. Cheung, 1980: Multiple-scattering effect on radiometric determinations of rain attenuation at millimeter wavelengths. Radio. Sci., 15, 507-516.

Kidder, S.Q., W.M. Gray, and T.H. Vonder Haar, 1978: Estimating tropical cyclone central pressure and outer winds from satellite microwave data. Mon. Wea. Rev., 106, 1458-1464.

Liebe, H.J., G.G. Gimmestad, and J.D. Hopponen, 1977: Atmospheric oxygen microwave spectrum--experiment versus theory. IEEE Trans. Ant. Prop., 25, 327-335.

Paris, J.F., 1971: Transfer of Thermal Microwaves in the Atmosphere. Report Dept. of Meteor., Texas A&M Univ., Vol. I, Grant. No. NASA NGR-44-001-098, 257 pp.

Rosenkranz, P.W., F.T. Barath, J.C. Blinn, E.S. Johnston, W.B. Lenoir, D.H. Staelin, and J.W. Waters, 1972: Microwave radiometric measurements of atmospheric temperature and water from an aircraft. J. Geophys. Res., 77, 5833-5844.

Rosenkranz, P.W., 1975: Shape of the 5 mm oxygen band in the atmosphere. IEEE Tran. Ant. Prop., 23, 498-506.

Rosenkranz, P.W., D.H. Staelin, and N.C. Grody, 1978: Typhoon June (1975) viewed by a scanning microwave spectrometer. J. Geophys. Res., 83, 1857-1868.

Savage, R.C. and J.A. Weinman, 1975: Preliminary calculations of the upwelling radiance from rainclouds at 37.0 and 19.35 GHz. Bul. Am. Meteor. Soc., 56, 1272-1274.

Smith, W.L., H.M. Woolf, P.G. Abel, C.M. Hayden, M. Chalfant, and N.C. Grody, 1974: Nimbus-5 data processing system. NOAA Tech. Memo. NESS 57, 99 pp.

Smith, W.L., H.M. Woolf, C.M. Hayden, D.Q. Wark, and L. McMillin, 1979: The TIROS-N operational vertical sounder. Bul. Am. Meteor. Soc., 60, 1177-1187.

Waters, J., K.F. Kunzi, R. L. Pettyjohn, R.K.L. Poon, and D.H. Staelin, 1975: Remote sensing of atmospheric temperature profiles with the Nimbus-5 microwave spectrometer. J. Atmos. Sci., 32, 1953-1959.

Wilheit, T.T., A.T.C. Chang, M.S.V. Rao, E.B. Rodgers and J.S. Theon, 1977: A satellite technique for quantitatively mapping rainfall rates over the ocean. J. Appl. Meteor., 16, 551-560.

(Continued from inside front cover)

NESS 61 The Measurement of Atmospheric Transmittance From Sun and Sky With an Infrared Vertical Sounder. W. L. Smith and H. B. Howell, September 1972, 16 pp. (COM-73-50020)

NESS 62 Proposed Calibration Target for the Visible Channel of a Satellite Radiometer. K. L. Coulson and H. Jacobowitz, October 1972, 27 pp. (COM-73-10143)

NESS 63 Verification of Operational SIRS B Temperature Retrievals. Harold J. Brodrick and Christopher M. Hayden, December 1972, 26 pp. (COM-73-50279)

NESS 64 Radiometric Techniques for Observing the Atmosphere From Aircraft. William L. Smith and Warren J. Jacob, January 1973, 12 pp. (COM-73-50376)

NESS 65 Satellite Infrared Soundings From NOAA Spacecraft. L. M. McMillin, D. Q. Wark, J.M. Siomkajlo, P. G. Abel, A. Werbowetzki, L. A. Lauritson, J. A. Pritchard, D. S. Crosby, H. M. Woolf, R. C. Luebbe, M. P. Weinreb, H. E. Fleming, F. E. Bittner, and C. M. Hayden, September 1973, 112 pp. (COM-73-50936/6AS)

NESS 66 Effects of Aerosols on the Determination of the Temperature of the Earth's Surface From Radiance Measurements at 11.2 m. H. Jacobowitz and K. L. Coulson, September 1973, 18 pp. (COM-74-50013)

NESS 67 Vertical Resolution of Temperature Profiles for High Resolution Infrared Radiation Sounder (HIRS). Y. M. Chen, H. M. Woolf, and W. L. Smith, January 1974, 14 pp. (COM-74-50230)

NESS 68 Dependence of Antenna Temperature on the Polarization of Emitted Radiation for a Scanning Microwave Radiometer. Norman C. Grody, January 1974, 11 pp. (COM-74-50431/AS)

NESS 69 An Evaluation of May 1971 Satellite-Derived Sea Surface Temperatures for the Southern Hemisphere. P. Krishna Rao, April 1974, 13 pp. (COM-74-50643/AS)

NESS 70 Compatibility of Low-Cloud Vectors and Rawins for Synoptic Scale Analysis. L. F. Hubert and L. F. Whitney, Jr., October 1974, 26 pp. (COM-75-50065/AS)

NESS 71 An Intercomparison of Meteorological Parameters Derived From Radiosonde and Satellite Vertical Temperature Cross Sections. W. L. Smith and H. M. Woolf, November 1974, 13 pp. (COM-75-10432)

NESS 72 An Intercomparison of Radiosonde and Satellite-Derived Cross Sections During the AMTEX. W. C. Shen, W. L. Smith, and H. M. Woolf, February 1975, 18 pp. (COM-75-10439/AS)

NESS 73 Evaluation of a Balanced 300-mb Height Analysis as a Reference Level for Satellite-Derived soundings. Albert Thomasell, Jr., December 1975, 25 pp. (PB-253-058)

NESS 74 On the Estimation of Areal Windspeed Distribution in Tropical Cyclones With the Use of Satellite Data. Andrew Timchalk, August 1976, 41 pp. (PB-261-971)

NESS 75 Guide for Designing RF Ground Receiving Stations for TIROS-N. John R. Schneider, December 1976, 126 pp. (PB-262-931)

NESS 76 Determination of the Earth-Atmosphere Radiation Budget from NOAA Satellite Data. Arnold Gruber, November 1977, 31 pp. (PB-279-633)

NESS 77 Wind Analysis by Conditional Relaxation. Albert Thomasell, Jr., January 1979.

NESS 78 Geostationary Operational Environmental Satellite/Data Collection System. July 1979, 86 pp. (PB-301-276)

NESS 79 Error Characteristics of Satellite-Derived Winds. Lester F. Hubert and Albert Thomasell, Jr. June 1979, 44 pp. (PB-300-754)

NESS 80 Calculation of Atmospheric Radiances and Brightness Temperatures in Infrared Window Channels of Satellite Radiometers. Michael P. Weinreb and Michael L. Hill, March 1980, 43 pp. (PB80 208-119)

NESS 81 Improved Algorithm for Calculation of UTM and Geodetic Coordinates. Jeff Dozier, September 1980, 21 pp. (PB81 132680)

NESS 82 The Effect of Precipitation on Microwave Soundings in Low Latitudes. Lester F. Hubert, Norman C. Grody, Andrew Timchalk, and William C. Shen, April 1981, 34 pp. (PB81 225062)

NESS 83 Atmospheric Sounding User's Guide. Adolf Werbowetzki, ed., April 1981, 82 pp. (PB81 230476)

NESS 84 Use of NOAA/AVHRR Visible and Near-Infrared Data for Land Remote Sensing. Stanley R. Schneider, David F. McGinnis Jr., James A. Gatlin, September 1981.

NESS 85 Transmittances for the TIROS Operational Vertical Sounder. M.P. Weinreb, H.E. Fleming, L.M. McMillin, and A.C. Neuendorffer, September 1981.

NESS 86 Statistical and Synoptic Evaluations of TIROS-N and NOAA-6 Retrievals. Harold J. Brodrick, Carmella Watkins, and Arnold Gruber, October 1981.

NESS 87 Satellite Observations of Variations in Northern Hemisphere Seasonal Snow Cover. Kenneth F. Dewey and Richard Heim, Jr. December 1981.

NOAA SCIENTIFIC AND TECHNICAL PUBLICATIONS

The National Oceanic and Atmospheric Administration was established as part of the Department of Commerce on October 3, 1970. The mission responsibilities of NOAA are to assess the socioeconomic impact of natural and technological changes in the environment and to monitor and predict the state of the solid Earth, the oceans and their living resources, the atmosphere, and the space environment of the Earth.

The major components of NOAA regularly produce various types of scientific and technical information in the following kinds of publications:

PROFESSIONAL PAPERS — Important definitive research results, major techniques, and special investigations.

CONTRACT AND GRANT REPORTS — Reports prepared by contractors or grantees under NOAA sponsorship.

ATLAS — Presentation of analyzed data generally in the form of maps showing distribution of rainfall, chemical and physical conditions of oceans and atmosphere, distribution of fishes and marine mammals, ionospheric conditions, etc.

TECHNICAL SERVICE PUBLICATIONS — Reports containing data, observations, instructions, etc. A partial listing includes data serials; prediction and outlook periodicals; technical manuals, training papers, planning reports, and information serials; and miscellaneous technical publications.

TECHNICAL REPORTS — Journal quality with extensive details, mathematical developments, or data listings.

TECHNICAL MEMORANDUMS — Reports of preliminary, partial, or negative research or technology results, interim instructions, and the like.

Information on availability of NOAA publications can be obtained from:

ENVIRONMENTAL SCIENCE INFORMATION CENTER (OA/D812)
ENVIRONMENTAL DATA AND INFORMATION SERVICE
NATIONAL OCEANIC AND ATMOSPHERIC ADMINISTRATION
U.S. DEPARTMENT OF COMMERCE
Rockville, MD 20852

NOAA--S/T 82-63